Molecular Cell

Article

The Hsp104 N-Terminal Domain Enables Disaggregase Plasticity and Potentiation

Graphical Abstract

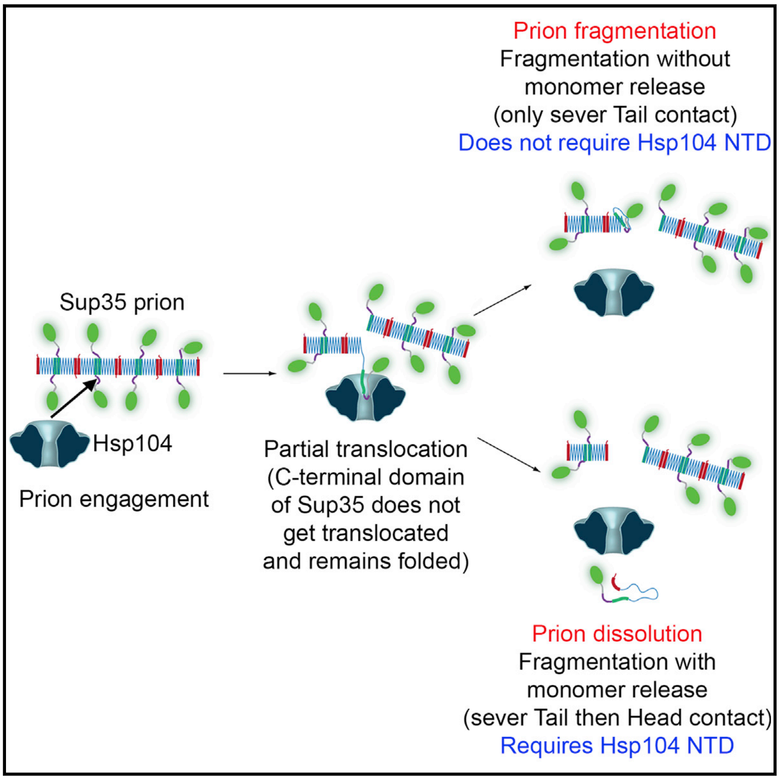

Highlights

- Hsp104 N-terminal domain confers plasticity that is critical for prion dissolution
- Detailed mechanism of how Hsp104 engages, fragments, and dissolves Sup35 prions
- SAXS reconstructions of Hsp104 hexamers reveal peristaltic pumping mechanism
- Hsp104 N-terminal domain is critical for activity of potentiated Hsp104 variants

Authors

Elizabeth A. Sweeny,
Meredith E. Jackrel, ..., Kushol Gupta,
James Shorter

Correspondence

jshorter@mail.med.upenn.edu

In Brief

Sweeny et al. employ small-angle X-ray scattering to reveal that a peristaltic pumping mechanism underpins Hsp104 disaggregase activity. They also define the mechanism by which Hsp104 dissolves Sup35 prions and elucidate that the Hsp104 N-terminal domain enables disaggregase plasticity and potentiation.

Sweeny et al., 2015, Molecular Cell *57*, 836–849
March 5, 2015
http://dx.doi.org/10.1016/j.molcel.2014.12.021

The Hsp104 N-Terminal Domain Enables Disaggregase Plasticity and Potentiation

Elizabeth A. Sweeny,[1,2,3] Meredith E. Jackrel,[1] Michelle S. Go,[1,4] Matthew A. Sochor,[1,2] Beatrice M. Razzo,[1] Morgan E. DeSantis,[1,2,5] Kushol Gupta,[1] and James Shorter[1,2,*]
[1]Department of Biochemistry and Biophysics
[2]Biochemistry and Molecular Biophysics Graduate Group
Perelman School of Medicine, University of Pennsylvania, Philadelphia, PA 19104, USA
[3]Present address: Department of Biological Engineering, Massachusetts Institute of Technology, Cambridge, MA 02139, USA
[4]Present address: Department of Medicine, University of North Carolina School of Medicine, Chapel Hill, NC 27599, USA
[5]Present address: Department of Cell Biology, Harvard Medical School, Boston, MA 02115, USA
*Correspondence: jshorter@mail.med.upenn.edu
http://dx.doi.org/10.1016/j.molcel.2014.12.021

SUMMARY

The structural basis by which Hsp104 dissolves disordered aggregates and prions is unknown. A single subunit within the Hsp104 hexamer can solubilize disordered aggregates, whereas prion dissolution requires collaboration by multiple Hsp104 subunits. Here, we establish that the poorly understood Hsp104 N-terminal domain (NTD) enables this operational plasticity. Hsp104 lacking the NTD (Hsp104$^{\Delta N}$) dissolves disordered aggregates but cannot dissolve prions or be potentiated by activating mutations. We define how Hsp104$^{\Delta N}$ invariably stimulates Sup35 prionogenesis by fragmenting prions without solubilizing Sup35, whereas Hsp104 couples Sup35 prion fragmentation and dissolution. Volumetric reconstruction of Hsp104 hexamers in ATPγS, ADP-AIF$_x$ (hydrolysis transition state mimic), and ADP via small-angle X-ray scattering revealed a peristaltic pumping motion upon ATP hydrolysis, which drives directional substrate translocation through the central Hsp104 channel and is profoundly altered in Hsp104$^{\Delta N}$. We establish that the Hsp104 NTD enables cooperative substrate translocation, which is critical for prion dissolution and potentiated disaggregase activity.

INTRODUCTION

Protein disaggregases hold potential to reverse protein aggregation and amyloidogenesis that underlie several fatal neurodegenerative disorders. Yet their structural and mechanistic basis of action is not understood. In yeast, a hexameric AAA+ protein, Hsp104, couples ATP hydrolysis to dissolution of disordered aggregates, preamyloid oligomers, and amyloid (Shorter, 2008). Curiously, metazoa lack an Hsp104 homolog. Thus, it could be valuable to translate these Hsp104 activities to counter neurodegenerative disease (Jackrel et al., 2014). In yeast, Hsp104 confers two major selective advantages (Shorter, 2008). First, Hsp104 confers tolerance to thermal and chemical stress by reactivating proteins trapped in disordered aggregates. Second, amyloid remodeling by Hsp104 enables yeast to deploy prions for adaptive purposes.

Hsp104 forms dynamic ring-shaped hexamers, which exchange subunits on the minute timescale (DeSantis et al., 2012; Wendler et al., 2007). Hsp104 harbors an N-terminal domain (NTD), two AAA+ nucleotide-binding domains (NBDs) that hydrolyze ATP, and a coiled-coil middle domain (MD) inserted in NBD1. Hsp104 drives protein disaggregation by coupling ATP hydrolysis to partial or complete substrate translocation across its central pore via interaction with conserved tyrosine-bearing pore loops (Shorter, 2008). Yet, the conformational changes of the hexamer and its central channel that drive substrate translocation are poorly resolved. Indeed, the hexameric structure of Hsp104 is unknown, and conflicting models have arisen from cryo-electron microscopy (EM) reconstructions of dysfunctional Hsp104 mutants in a limited number of nucleotide states (Carroni et al., 2014; Lee et al., 2010; Wendler et al., 2007, 2009).

Hsp104 hexamers exhibit mechanistic plasticity and adapt distinct modes of intersubunit collaboration to disaggregate disordered aggregates versus amyloid. To disaggregate disordered aggregates, Hsp104 subunits within the hexamer collaborate noncooperatively via probabilistic substrate binding and ATP hydrolysis (DeSantis et al., 2012). By contrast, to resolve stable amyloid, several Hsp104 subunits within the hexamer cooperatively engage substrate and hydrolyze ATP (DeSantis et al., 2012). How this switch from noncooperative to cooperative mechanism occurs is not understood.

Hsp104 activity is potentiated by specific mutations in the MD (Jackrel et al., 2014). Potentiating mutations enable Hsp104 to dissolve fibrils formed by neurodegenerative disease proteins, including TDP-43, FUS, and α-synuclein (α-syn), and mitigate neurodegeneration under conditions where wild-type (WT) Hsp104 is inactive (Jackrel et al., 2014). These mutations reconfigure how Hsp104 subunits collaborate and increase plasticity such that robust disaggregase activity is maintained despite diverse subunit-inactivating events (Jackrel et al., 2014). The precise domain requirements that underpin potentiation as well as operational plasticity are unknown.

Cell Press

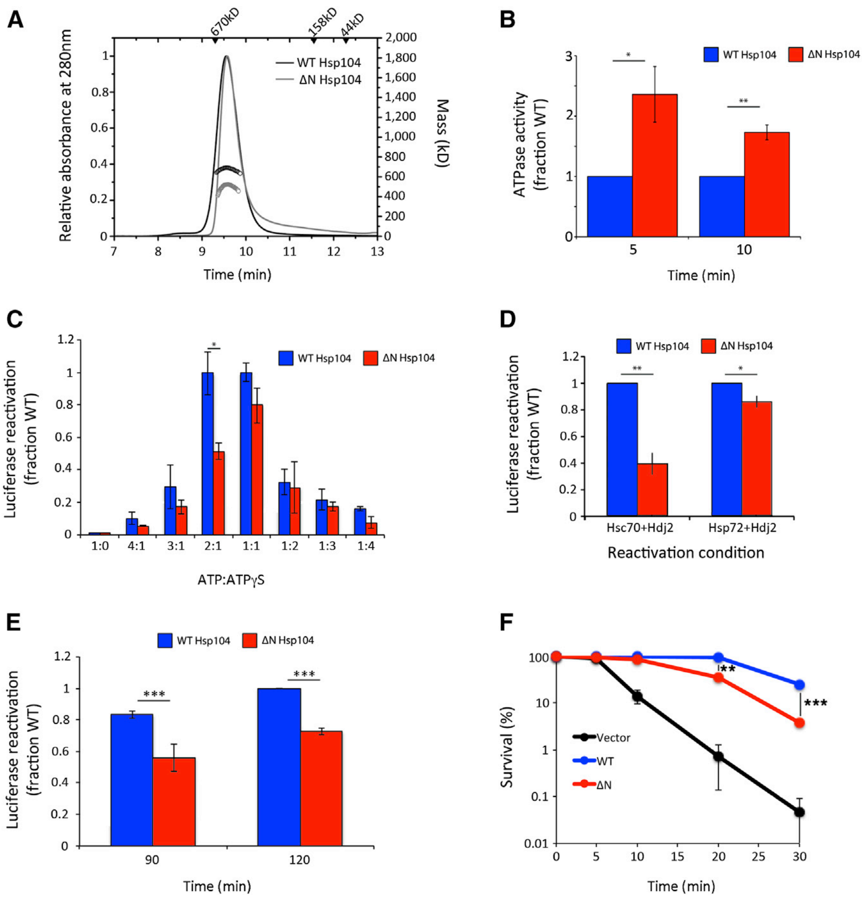

Figure 1. Hsp104$^{\Delta N}$ Has Reduced Disaggregase Activity

(A) Size-exclusion chromatography coupled to multiangle light scattering demonstrates that Hsp104 and Hsp104$^{\Delta N}$ form hexamers. A representative data set from three experiments is shown.

(B) Hsp104$^{\Delta N}$ exhibits elevated ATPase activity compared to Hsp104. Values represent means ± SEM (n = 3–4; *$p < 0.05$; **$p < 0.01$, two-tailed t test).

(C) Luciferase aggregates were treated with Hsp104 or Hsp104$^{\Delta N}$ plus various ATP:ATPγS ratios. Values represent means ± SEM (n = 3; *$p < 0.05$, two-tailed t test).

(D) Luciferase aggregates were treated with Hsp104 or Hsp104$^{\Delta N}$ with ATP plus Hdj2 and Hsp72 or Hdj2 and Hsc70. Values represent means ± SEM (n = 3–7; *$p < 0.05$; **$p < 0.01$, two-tailed t test).

(E) Δ*hsp104* yeast expressing luciferase and Hsp104 or Hsp104$^{\Delta N}$ were shifted to 44°C, treated with cycloheximide, and allowed to recover at 30°C. Luciferase activity (% WT control) was determined. Values represent means ± SEM (n = 3; ***$p < 0.001$, two-tailed t test).

(F) Δ*hsp104* yeast harboring empty vector or expressing Hsp104 or Hsp104$^{\Delta N}$ were treated at 37°C for 30 min and then 50°C for 0–30 min. Cells were plated and survival (%) calculated. Values represent means ± SEM (n = 3; **$p < 0.01$; ***$p < 0.001$, two-tailed t test).

Hsp104 harbors an NTD of poorly defined function, which is considered dispensable (Hung and Masison, 2006; Lum et al., 2008). The NTD of ClpB, the *E. coli* Hsp104 homolog, contributes to substrate binding and disordered aggregate dissolution (Barnett et al., 2005). However, several facets of Hsp104 activity are not conserved from ClpB (DeSantis et al., 2012, 2014). Unlike Hsp104, ClpB has limited ability to dissolve amyloid (DeSantis et al., 2012). Thus, whether NTD function is conserved from ClpB to Hsp104 is unclear. Indeed, replacing the Hsp104 NTD with the ClpB NTD disrupts prion propagation (Tipton et al., 2008). Hsp104 lacking the NTD (Hsp104$^{\Delta N}$) supports [*PSI*$^{+}$] (Sup35 prion) inheritance, which requires Sup35 prion fragmentation (Hung and Masison, 2006). Curiously, unlike Hsp104, overexpression of Hsp104$^{\Delta N}$ does not cure or inefficiently cures [*PSI*$^{+}$] depending upon genetic background (Hung and Masison, 2006; Park et al., 2014). The direct effects of Hsp104$^{\Delta N}$ on Sup35 prionogenesis are unknown.

Here, we define critical NTD functions in enabling Hsp104 plasticity and potentiation. Using pure components, we establish that Hsp104$^{\Delta N}$ dissolves disordered aggregates but not prions. In contrast to Hsp104, which breaks N- and C-terminal intermolecular prion contacts to release soluble Sup35 and eliminate cross-β structure, Hsp104$^{\Delta N}$ only breaks C-terminal intermolecular prion contacts and fragments Sup35 prions without solubilizing Sup35 or resolving cross-β structure. These differences reflect profound alterations in how Hsp104 and Hsp104$^{\Delta N}$ hexamers coordinate substrate translocation. Indeed, the Hsp104 NTD enables cooperative substrate translocation by Hsp104, which is critical for potentiated activity and prion dissolution, but not for prion fragmentation.

RESULTS

Hsp104$^{\Delta N}$ Has Reduced Disaggregase Activity

Deletion of the Hsp104 NTD is reported to have minimal effect on disaggregase functionality (Hung and Masison, 2006; Lum et al., 2008). This is not what we found. Hsp104$^{\Delta N}$ was hexameric and had elevated ATPase activity (Figures 1A and 1B). Hsp104 and Hsp104$^{\Delta N}$ solubilized disordered aggregates without Hsp70 and Hsp40 when provided with mixtures of ATP and ATPγS, a slowly hydrolyzable ATP analog (Figure 1C). However, at every ATP:ATPγS ratio tested, Hsp104$^{\Delta N}$ was slightly less active than Hsp104 (Figure 1C). At 2 ATP:1 ATPγS, Hsp104 was optimally activated, but Hsp104$^{\Delta N}$ was only ~50% active (Figure 1C). This distinct sensitivity to activation by ATPγS suggests that Hsp104$^{\Delta N}$ hexamers are tuned differently than Hsp104 hexamers. Specifically, under these conditions, Hsp104$^{\Delta N}$ hexamers require more ATPγS relative to ATP for maximal disaggregase activity (Figure 1C).

Compared to Hsp104, Hsp104$^{\Delta N}$ displayed reduced disaggregase activity with different Hsp70s (Figure 1D). This deficit was most pronounced for Hsc70 and significant for Hsp72 (Figure 1D). Hsp104$^{\Delta N}$ had reduced ability to disaggregate luciferase and confer thermotolerance in vivo (Figures 1E and 1F), despite

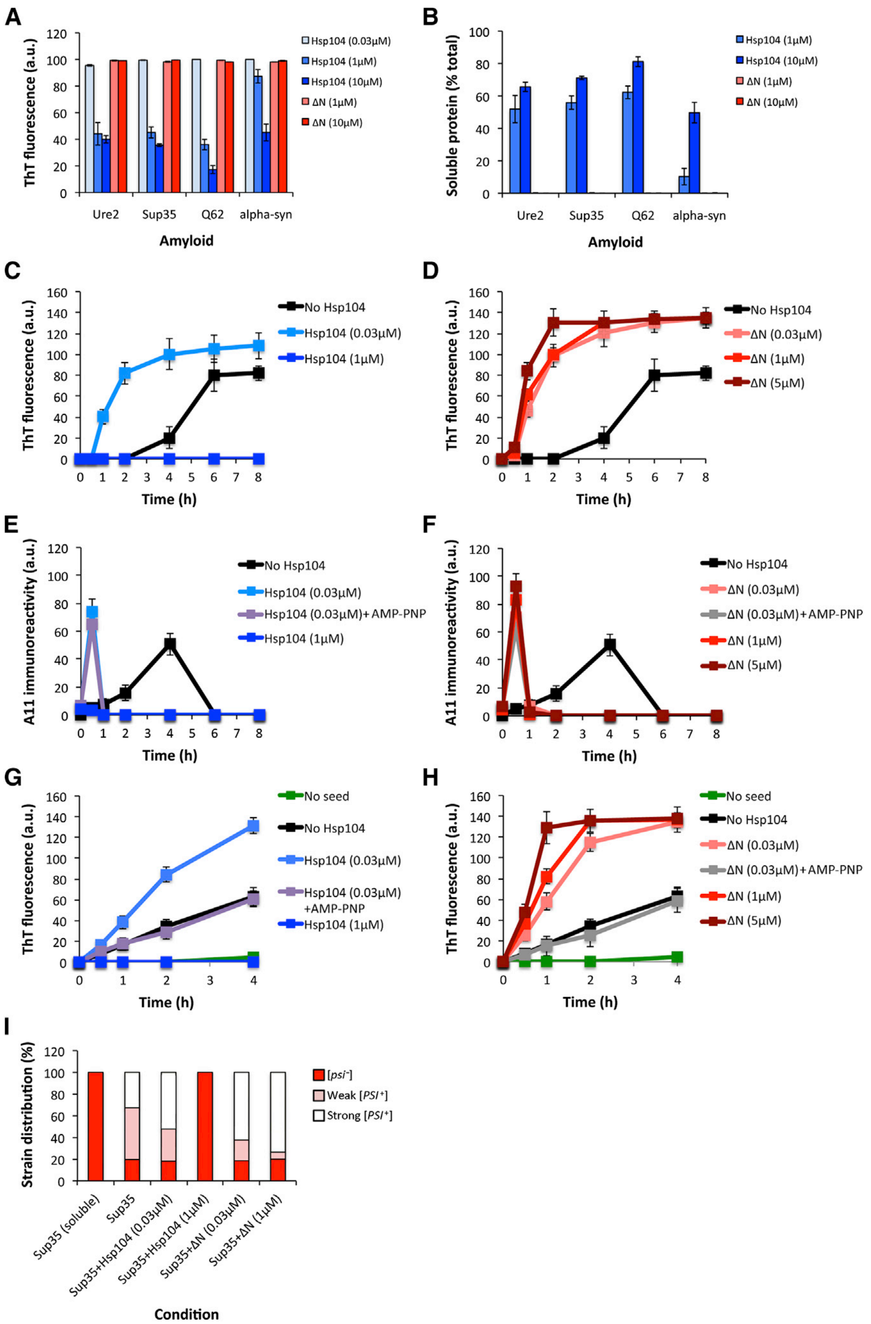

Figure 2. Hsp104$^{\Delta N}$ Cannot Dissolve Amyloid and Invariably Promotes Sup35 Prionogenesis

(A and B) Sup35 or Ure2 prions, or Q62 or α-syn amyloid, were treated with Hsp104 or Hsp104$^{\Delta N}$ plus Ssa1, Sse1, and Sis1. Fiber integrity was assessed by ThT fluorescence (A) or sedimentation analysis (B). Values represent means ± SEM (n = 3).

(C and D) Kinetics of unseeded Sup35 prionogenesis without or with Hsp104 (C) or Hsp104$^{\Delta N}$ (D) assessed by ThT fluorescence. Values represent means ± SEM (n = 3).

(E and F) Unseeded Sup35 prionogenesis plus or minus Hsp104 (E) or Hsp104$^{\Delta N}$ (F). In some reactions, ATP was replaced with AMP-PNP. At various times, the amount of A11-reactive species was determined. Values represent means ± SEM (n = 3).

(G and H) Kinetics of Sup35 prionogenesis seeded by Sup35 prions plus or minus Hsp104 (G) or Hsp104$^{\Delta N}$ (H) assessed by ThT fluorescence. In some reactions, ATP was replaced with AMP-PNP. Values represent means ± SEM (n = 3).

(I) Reactions were performed as in (C) and (D). Reaction products were sonicated and transformed into [*psi*$^-$] cells. The proportion of [*psi*$^-$], weak [*PSI*$^+$], and strong [*PSI*$^+$] colonies was determined. Values represent means (n = 3).

See also Table S1.

similar expression levels to Hsp104. Thus, deletion of the Hsp104 NTD reduces disaggregase activity in vitro and in vivo.

Hsp104 dissolves disordered aggregates via a noncooperative mechanism that does not require collaboration between Hsp104 subunits within the hexamer. Indeed, a single active Hsp104 subunit within the hexamer can drive disaggregation (DeSantis et al., 2012). By contrast, amyloid dissolution requires cooperative ATP hydrolysis and substrate binding by several Hsp104 subunits (DeSantis et al., 2012). In contrast to Hsp104, which disaggregated Sup35, Ure2, polyglutamine, and α-syn amyloid, Hsp104$^{\Delta N}$ was ineffective even at high concentrations (Figures 2A and 2B). Strikingly, Hsp104$^{\Delta N}$ did not release soluble protein (Figure 2B), which helps explain why Hsp104$^{\Delta N}$ overexpression fails to cure Sup35 prions in some genetic backgrounds (Hung and Masison, 2006). The inability of Hsp104$^{\Delta N}$ to disaggregate amyloid was not due to reduced binding affinity (see Table S1 available online). Thus, after initial engagement, some aspect of amyloid antagonizes Hsp104$^{\Delta N}$, but not Hsp104. We suggest that Hsp104$^{\Delta N}$ subunits are unable to function in a globally cooperative manner to resolve amyloid.

Hsp104$^{\Delta N}$ Only Stimulates Sup35 Prionogenesis

We investigated the interaction between Hsp104$^{\Delta N}$ and Sup35 further. Thus, we titrated Hsp104$^{\Delta N}$ into de novo Sup35 prionogenesis in vitro, which is very sensitive to Hsp104 concentration. At low concentrations, Hsp104 stimulates spontaneous Sup35 prionogenesis by reducing lag phase and accelerating assembly phase (Figure 2C). At high concentrations, Hsp104 inhibits Sup35 prionogenesis (Figure 2C) (Shorter and Lindquist, 2006). By contrast, even at very high concentrations, Hsp104$^{\Delta N}$ stimulated spontaneous Sup35 prionogenesis by reducing lag phase and accelerating assembly phase (Figure 2D). Thus, deletion of the Hsp104 NTD drastically alters the concentration-dependent effect of Hsp104 on Sup35 prionogenesis, such that inhibition of prion formation is diminished. Indeed, the absence of the NTD switches Hsp104 to an operating mode that stimulates Sup35 prionogenesis.

Stimulation of spontaneous Sup35 prionogenesis by low concentrations of Hsp104 is due to two activities (Shorter and Lindquist, 2006). First, Hsp104 reduces lag phase by accelerating formation of prionogenic Sup35 oligomers, which are recognized by an anti-oligomer antibody, A11. This activity requires ATP binding but not hydrolysis by Hsp104. Second, Hsp104 accelerates assembly phase by occasionally fragmenting Sup35 prions to generate additional fibril ends for conformational replication. This activity requires ATP hydrolysis by Hsp104.

We assessed the effect of Hsp104$^{\Delta N}$ on prionogenic Sup35 oligomer formation. Sup35 slowly formed A11-reactive oligomers that peaked at the end of lag phase (~4 hr) and rapidly disappeared during assembly phase (Figure 2E). High concentrations of Hsp104 prevented formation of A11-reactive species, whereas low concentrations of Hsp104 stimulated their appearance at 30 min, after which A11-reactive oligomers disappeared upon rapid prionogenesis (Figures 2C and 2E) (Shorter and Lindquist, 2006). By contrast, low and high concentrations of Hsp104$^{\Delta N}$ accelerated A11-reactive oligomer formation (Figures 2D and 2F). This acceleration did not require ATP hydrolysis and was supported by a nonhydrolyzable ATP analog, AMP-PNP (Figures 2E and 2F). Thus, the Hsp104 NTD is not required to accelerate prionogenic oligomer formation, but is essential for high concentrations of Hsp104 to inhibit Sup35 oligomer formation.

To assess how Hsp104$^{\Delta N}$ affected assembly phase, we titrated it into Sup35 prionogenesis seeded by Sup35 prions. At low concentrations, Hsp104 accelerated seeded Sup35 assembly and was inhibited by AMP-PNP (Figure 2G). At high concentrations, Hsp104 inhibited seeded Sup35 assembly (Figure 2G). By contrast, even at high concentrations, Hsp104$^{\Delta N}$ accelerated seeded Sup35 prionogenesis (Figure 2H). Acceleration by Hsp104$^{\Delta N}$ required ATP hydrolysis, and was inhibited by AMP-PNP (Figure 2H). Thus, Hsp104$^{\Delta N}$ fragments Sup35 prions but is unable to dissolve them (Figures 2A and 2B). Indeed, prion fragmentation and dissolution are uncoupled by deletion of the Hsp104 NTD.

Hsp104$^{\Delta N}$ Promotes Formation of Sup35 Prions that Encode Strong [*PSI*$^+$]

Sup35 forms distinct cross-β structures or "strains," which encode distinct [*PSI*$^+$] phenotypes designated "weak" or "strong" to describe the magnitude of Sup35 loss of function. We assessed how Hsp104 and Hsp104$^{\Delta N}$ altered Sup35 prion strain distribution. Thus, we infected [*psi*$^-$] yeast with Sup35 prions formed in the presence of Hsp104 or Hsp104$^{\Delta N}$. Sup35 prions formed without Hsp104 gave rise to ~40% strong [*PSI*$^+$] and ~60% weak [*PSI*$^+$] (Figure 2I). Low concentrations of Hsp104 shifted the population toward strong [*PSI*$^+$], ~63% strong [*PSI*$^+$] and ~37% weak [*PSI*$^+$], whereas a higher Hsp104 concentration (1 μM) prevented Sup35 prionogenesis (Figure 2I). By contrast, low concentrations of Hsp104$^{\Delta N}$ (0.03 μM) significantly shifted the population toward strong [*PSI*$^+$]: ~76% strong [*PSI*$^+$] and ~24% weak [*PSI*$^+$] (Figure 2I; $p < 0.05$, two-tailed t test). Higher Hsp104$^{\Delta N}$ concentration exacerbated this effect: ~92% strong [*PSI*$^+$] and ~8% weak [*PSI*$^+$] (Figure 2I). Thus, the altered activity of Hsp104$^{\Delta N}$ accentuates prion strain selection events that favor strong [*PSI*$^+$]. Indeed, Hsp104$^{\Delta N}$ "strengthens" [*PSI*$^+$] phenotypes in vivo (Hung and Masison, 2006).

Hsp104$^{\Delta N}$ Fragments Sup35 Prions by Selectively Breaking Tail Contacts

To assess prion-fragmenting activity of Hsp104$^{\Delta N}$, we treated Sup35 prions with low or high concentrations of Hsp104$^{\Delta N}$ or Hsp104. Low concentrations of Hsp104 fragmented Sup35 prions as revealed by EM (Figure 3A), without reducing ThT fluorescence (Figure 2A). Fragmentation was confirmed by the ability of remodeled products to seed Sup35 prionogenesis (Figure 3B) or infect [*psi*$^-$] yeast (Figure 3C). High concentrations of Hsp104 eliminated Sup35 prions (Figures 2A and 3A–3C). By contrast, low or high concentrations of Hsp104$^{\Delta N}$ fragmented Sup35 prions and enhanced their seeding activity without eliminating them (Figures 3A–3C). EM revealed long tracks of closely aligned short fibrils, as though Hsp104$^{\Delta N}$ had fragmented a long fibril at several positions along its course (Figure 3A, asterisks). Treatment of Sup35 prions with low concentrations of Hsp104 or any concentration of Hsp104$^{\Delta N}$ amplified strong [*PSI*$^+$] prions (Figure 3C). This effect was most pronounced at high Hsp104$^{\Delta N}$ concentrations (Figure 3C). Thus, the Hsp104 NTD is essential to dissolve Sup35 prions.

To determine how Hsp104$^{\Delta N}$ fragments Sup35 prions, we monitored intermolecular prion contacts. We employed the N-terminal prion domain (N, residues 1–121) and MD (M, residues 122–253) of Sup35, termed NM (Figure 3D). We assembled NM prions at 4°C to yield the prion ensemble NM4, which encodes predominantly strong [*PSI*$^+$] (DeSantis and Shorter, 2012). Specifically, we assembled NM4 prions with 17 individual single cysteine NM variants labeled with pyrene at different positions. These pyrene-labeled NM variants retain WT assembly kinetics and infectivity, indicating that pyrene does not significantly alter prion structure (Krishnan and Lindquist, 2005). Upon intermolecular contact formation, pyrene molecules at select positions, in the "Head" or "Tail" (Figures 3D and 3E), form excimers (excited-state dimers) that produce a strong red shift in fluorescence. Excimer fluorescence reports on intermolecular contact integrity, and NM prions are held together by intermolecular Head-to-Head and Tail-to-Tail contacts (Figure 3D) (Krishnan and Lindquist, 2005).

High concentrations of Hsp104 disrupted Head (residues 21–38) and Tail (residues 79–96) contacts of NM4 prions, whereas the low Hsp104 concentration also disrupted both contacts, but to a lesser extent (Figure 3E). By contrast, Hsp104$^{\Delta N}$ only disrupted Tail contacts even at high concentrations (Figure 3E). Thus, the NTD is not required for Hsp104 to break the Tail contact, but is critical to break the Head contact and dissolve Sup35 prions.

Hsp104 Breaks the Tail Contact and then the Head Contact of Sup35 Prions

To understand the selective breakage of Tail contacts by Hsp104$^{\Delta N}$, we tracked NM4 prion remodeling kinetics. The "double Walker B" (DWB, E285Q:E687Q) Hsp104 mutant, which can bind but not hydrolyze ATP, failed to break Head or Tail contacts (Figure 3F). At early times (0–10 min), Hsp104 and

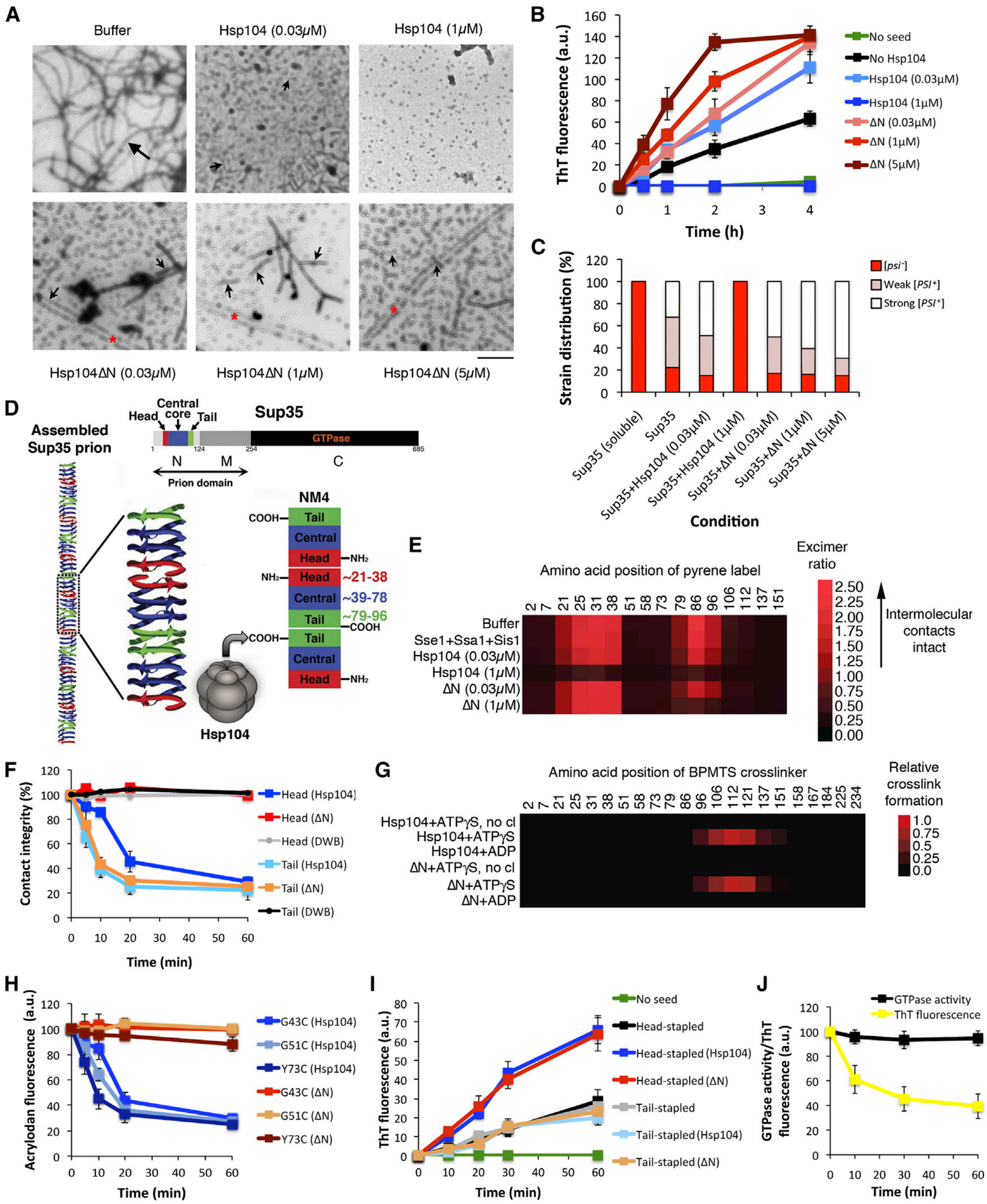

Figure 3. Hsp104$^{\Delta N}$ Fragments Sup35 Prions by Selectively Breaking Tail Contacts

(A) Sup35 prions were treated with buffer, Hsp104, or Hsp104$^{\Delta N}$ plus Sse1, Ssa1, and Sis1 for 1 hr and processed for EM. Note the long fibrils in buffer control (large arrow), shorter fibrils (small arrows) in the presence of Hsp104$^{\Delta N}$ or Hsp104 (0.03 μM), and absence of fibrils with Hsp104 (1 μM). Asterisks denote long tracks of closely aligned short fibrils. Scale bar, 0.5 μm.

(B) Sup35 prions were left untreated, sonicated, or treated with His$_6$-Hsp104 or His$_6$-Hsp104$^{\Delta N}$ plus Sse1, Ssa1, and Sis1 for 1 hr. Reactions were depleted of His$_6$-Hsp104 or His$_6$-Hsp104$^{\Delta N}$ and used to seed (2% wt/wt) Sup35 prionogenesis assessed by ThT fluorescence. Values represent means ± SEM (n = 3).

(C) Sup35 prions were treated as in (A), and reaction products were sonicated and transformed into [*psi*⁻] cells. The proportion of [*psi*⁻], weak [*PSI*⁺], and strong [*PSI*⁺] colonies was determined. Values represent means (n = 3).

(D) Sup35 harbors a C-terminal GTPase domain (residues 254–685, black), a charged middle domain (M, residues 124–253, dark gray), and a prionogenic N-terminal domain (N, residues 1–123, light gray). Within N, prion recognition elements make homotypic intermolecular contacts, and Sup35 prions are maintained by Head-to-Head (red) and Tail-to-Tail (green) contacts. A central core (blue) is sequestered by intramolecular contacts. Head, central core, and Tail position are shown for NM4 prions. Hsp104 engages Sup35 prions C-terminal to the Tail contact.

(legend continued on next page)

$Hsp104^{\Delta N}$ broke the Tail contact (G86C), whereas the Head contact (G31C) remained intact (Figure 3F). At later times (20–60 min), Hsp104 severed Head contacts, but $Hsp104^{\Delta N}$ did not (Figure 3F). Thus, Hsp104 breaks the Tail and then the Head contact to remodel NM4 prions. This temporal separation suggested that Hsp104 and $Hsp104^{\Delta N}$ engage NM4 prions C-terminal to the Tail contact and then exert a directional pulling force that first breaks the Tail contact (Figure 3D). However, $Hsp104^{\Delta N}$ is unable to melt cross-β structure N-terminal to the Tail and releases after the Tail contact is broken but before the Head contact is broken. By contrast, Hsp104 breaks the Tail contact and continues to translocate NM sequence along a C- to N-terminal vector, thereby melting cross-β structure of the central core and then breaking the Head contact. To test this model, we performed three experiments.

First, we assessed where Hsp104 and $Hsp104^{\Delta N}$ initially engage NM4 prions. Thus, single cysteine NM variants labeled with a cleavable thiol-specific UV-activatable 13Å crosslinker, benzophenone-4-carboxamidocysteine methanethiosulphonate (BPMTS), were assembled into NM4 prions. BPMTS-labeled NM variants retain WT assembly kinetics and infectivity (Figures S1A and S1B), indicating that BPMTS does not affect prionogenesis. BPMTS-labeled NM4 prions were incubated with Hsp104 or $Hsp104^{\Delta N}$ plus ATPγS (to favor binding) or ADP (to disfavor binding) and crosslinked. Neither Hsp104 nor $Hsp104^{\Delta N}$ was recovered without crosslinking or with ADP (Figure 3G). By contrast, with ATPγS, Hsp104 and $Hsp104^{\Delta N}$ were recovered only when BPMTS was attached at positions 96, 106, 112, 121, 137, and 151 (Figure 3G). Thus, Hsp104 and $Hsp104^{\Delta N}$ initially engage NM4 prions C-terminal to the Tail contact, in a region spanning residues 96–151 (Figure 3D). Subsequently, $Hsp104^{\Delta N}$ breaks the Tail contact and fragments the prion, but is unable to release soluble NM, which requires unfolding the central core and severing the Head contact, a task accomplished by Hsp104.

Second, we tracked the central core between the Head and Tail. Thus, we employed single cysteine NM variants bearing acrylodan labels at G43C, G51C, or Y73C, which lie in the central core (Figure 3D). Sequestration of labeled sites from solvent in the assembled prion increases acrylodan fluorescence at these positions (Krishnan and Lindquist, 2005). $Hsp104^{\Delta N}$ failed to alter acrylodan fluorescence of NM4 prions (Figure 3H). Thus, $Hsp104^{\Delta N}$ does not remodel the central core. By contrast, Hsp104 reduced acrylodan fluorescence at these positions, indicating that the central core was remodeled and exposed to solvent (Figure 3H). Hsp104-driven unfolding of the central core was not concerted but occurred in a stepwise manner. Thus, the Y73 position displayed changes prior to G51 and G43, indicating that Hsp104 remodels C-terminal portions of the central core prior to N-terminal portions (Figure 3H). Thus, Hsp104 breaks the Tail contact and then unfolds the central core by pulling on its C-terminal end.

Third, we assembled NM prions from single cysteine NM variants that were stapled together at the Head (N21C) or Tail (G96C) contact by an 11Å crosslinker 1,4-bis-maleimidobutane (BMB) (Krishnan and Lindquist, 2005). NM4 prions stapled at the Head contact could be fragmented by Hsp104 and $Hsp104^{\Delta N}$ and were more potent seeds than untreated NM4 prions (Figure 3I). By contrast, NM prions stapled at the Tail contact could not be fragmented by Hsp104 or $Hsp104^{\Delta N}$ and seeded NM assembly just as well as untreated prions (Figure 3I). Thus, Hsp104 cannot break the Head contact until after the Tail contact has been broken.

NM lacks the C-terminal GTPase domain of Sup35 (Figure 3D). Does Hsp104 need to unfold the C-terminal GTPase domain to dissolve Sup35 prions? Full-length Sup35 retains similar GTPase activity in the prion and soluble state (Krzewska et al., 2007). Thus, to assess whether the Sup35 C-terminal domain was unfolded during Hsp104-catalzed prion dissolution, we included $GroEL_{TRAP}$, which captures unfolded protein and prevents refolding. Hsp104 disassembled Sup35 prions, but GTPase activity was unchanged (Figure 3J), indicating that Hsp104 dissolves Sup35 prions without unfolding the C-terminal GTPase domain. Likewise, Hsp104 did not unfold GFP during dissolution of NM-GFP prions (Figures S1C and S1D). Thus, Hsp104 selectively resolves N-terminal prion structure without unfolding the appended C-terminal domain.

$Hsp104^{\Delta N}$ Has Impaired Translocation and Unfoldase Activity

The inability to resolve cross-β structure or break Head contacts of NM4 prions suggested that $Hsp104^{\Delta N}$ might be defective in substrate translocation and unfolding. Indeed, FITC-casein degradation and $RepA_{1-70}$-GFP unfolding assays confirmed that $Hsp104^{\Delta N}$ has impaired translocation and unfoldase activity (Figures S1E and S1F).

(E) NM4 prions carrying pyrene labels at the indicated single site were treated with Hsp104 or $Hsp104^{\Delta N}$ plus Sse1, Ssa1, and Sis1 for 1 hr. The ratio of excimer to nonexcimer fluorescence (I_{465nm}/I_{375nm}) was then determined. Values represent means (n = 3).
(F) NM4 prions carrying pyrene labels in the Head (G31C) or Tail (G86C) were incubated with Hsp104, $Hsp104^{\Delta N}$, or $Hsp104^{DWB}$ (1 μM) plus Sse1, Ssa1, and Sis1 for 0–1 hr. At various times, the ratio of excimer to nonexcimer fluorescence (I_{465nm}/I_{375nm}) was determined and compared to the zero time point to determine contact integrity (%). Values represent means ± SEM (n = 3).
(G) Mapping contact sites between NM4 prions and Hsp104+ATPγS, Hsp104+ADP, $Hsp104^{\Delta N}$+ATPγS, and $Hsp104^{\Delta N}$+ADP by site-resolved BPMTS crosslinking. Heatmap displays positions where Hsp104 was crosslinked to NM4 prions. No cl (no crosslinking control). Values represent means (n = 3).
(H) NM4 prions carrying acrylodan labels in the central core (G43C, G51C, or Y73C) were treated with Hsp104 or $Hsp104^{\Delta N}$ (1 μM) plus Sse1, Ssa1, and Sis1 for 0–1 hr. At the indicated times, acrylodan fluorescence was measured. Values represent means ± SEM (n = 3).
(I) NM prions (2.5 μM monomer) crosslinked by BMB in the Head (N21C) or Tail (G96C) were left untreated or treated with His_6-Hsp104 (1 μM) or His_6-$Hsp104^{\Delta N}$ (1 μM) plus Sse1, Ssa1, and Sis1 for 1 hr. Reactions were depleted of His_6-Hsp104 or His_6-$Hsp104^{\Delta N}$ and used to seed (2% wt/wt) NM prionogenesis assessed by ThT fluorescence. Values represent means ± SEM (n = 3).
(J) Sup35 prions were treated with Hsp104 (1 μM) plus $GroEL_{TRAP}$, Sse1, Ssa1, and Sis1 for 0–1 hr. At various times, GTPase activity and ThT fluorescence were measured. Values represent means ± SEM (n = 3).
See also Figure S1.

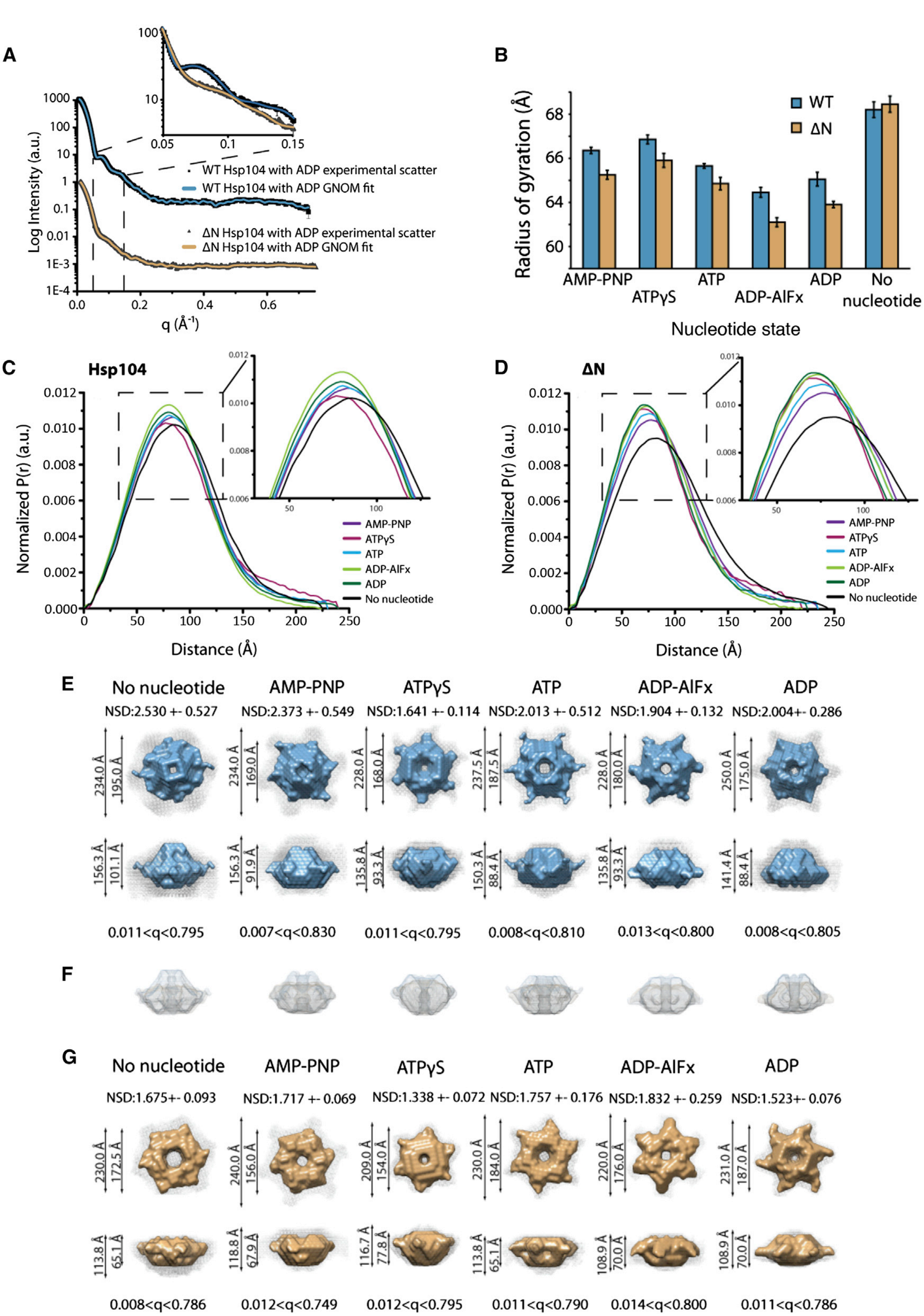

Figure 4. NTD Deletion Alters ATPase-Driven Conformational Changes of Hsp104 Hexamers

(A) Representative scattering profiles for Hsp104 and Hsp104$^{\Delta N}$ (intensity versus momentum transfer, q [Å^{-1}]). Profiles are arbitrarily scaled on the y axis for better visualization. Inset shows enlargement of regions where Hsp104 consistently differs from Hsp104$^{\Delta N}$ in all nucleotide states. Experimental data are overlaid by GNOM fit.

(legend continued on next page)

NTD Deletion Alters ATPase-Driven Conformational Changes of Hsp104 Hexamers

To understand the differences between Hsp104 and Hsp104$^{\Delta N}$ at a structural level, we examined changes in shape of Hsp104 and Hsp104$^{\Delta N}$ hexamers through the ATPase cycle in solution using small- and wide-angle X-ray scattering (SAXS/WAXS). X-ray scattering at very low angles provides information about particle size and shape. Hsp104 and Hsp104$^{\Delta N}$ were hexameric and monodisperse in solution and ideally suited for SAXS (Figure 1A; and see calculated mass of particle [MM by Qr] in Table S2). We measured scattering at multiple concentrations and different beamlines and obtained very similar results (Table S2). Guinier analysis confirmed the absence of aggregation or other concentration-dependent effects (Figure S2A) (Volkov and Svergun, 2003). Thus, we determined structural parameters of Hsp104 and Hsp104$^{\Delta N}$, including maximum dimension (D_{max}) and radius of gyration (R_g) in six nucleotide states—AMP-PNP, ATPγS, ATP, ADP-AlF$_x$ (ATP hydrolysis transition state mimic), ADP, and no nucleotide—to simulate the steps of the ATP hydrolysis cycle. Data were measured to a q_{max} of ~0.7–0.8 Å^{-1} to yield a nominal resolution limit ($2\pi/q_{max}$) of 7.6–8.4 Å.

Raw scattering profiles (I[q] versus q, where $q = 4\pi[\sin\theta]/\lambda$) and GNOM (Svergun, 1992) fits to experimental data revealed large differences between Hsp104 and Hsp104$^{\Delta N}$ (Figure 4A). Distinctive features in the low q region present in Hsp104, but not Hsp104$^{\Delta N}$ (corresponding to the NTD), are highlighted (Figure 4A, inset). In the absence of nucleotide, Hsp104 and Hsp104$^{\Delta N}$ hexamers have their largest R_g and D_{max} (Figure 4B; Tables S2 and S3). Addition of nucleotide decreased R_g and D_{max} (Figure 4B; Tables S2 and S3). For Hsp104 and Hsp104$^{\Delta N}$, AMP-PNP and ATPγS elicited larger spatial properties (Figure 4B; Tables S2 and S3). ADP-AlF$_x$, which mimics the ATP hydrolysis transition state, where ADP and Pi are bound, yielded the smallest R_g and D_{max} values for Hsp104 and Hsp104$^{\Delta N}$ (Figure 4B; Tables S2 and S3). The spatial properties of Hsp104 and Hsp104$^{\Delta N}$ then expand slightly upon Pi release in the ADP state (Figure 4B; Table S3). Thus, Hsp104 and Hsp104$^{\Delta N}$ hexamers contract upon ATP hydrolysis and expand upon ATP binding (Figure 4B; Tables S2 and S3), indicating a pumping mechanism to drive substrate translocation.

Structural changes of Hsp104 and Hsp104$^{\Delta N}$ hexamers were evident in the real-space pairwise distance distribution function, or P(r), which represents the distances between pairs of atoms within a given volume. As with R_g, the apparent redistribution of interatomic vectors in the P(r) curves demonstrates that nucleotide addition and identity induce specific changes in shape for Hsp104 and Hsp104$^{\Delta N}$ hexamers (Figures 4C and 4D). How the Hsp104 hexamer responds to a given nucleotide, both in terms of the magnitude and the specific effect, differs in the absence of the NTD (Figures 4C and 4D).

To visualize these changes, we employed the ab initio modeling program GASBOR (Svergun et al., 2001) to derive volumetric reconstructions of the averaged solution shape of Hsp104 and Hsp104$^{\Delta N}$ hexamers with each nucleotide. GASBOR employs simulated annealing to match experimental scattering data with an ensemble of beads corresponding to the composition of the particle. For each nucleotide, GASBOR calculations were performed ten times using scattering data to q_{max} of 0.7–0.8 Å^{-1} (nominal resolution limit of 7.6–8.4 Å). GASBOR calculations using q_{max} truncated to 0.5 Å^{-1} or calculations with the program DAMMIN/F yielded similar results. We imposed 6-fold symmetry based upon cryo-EM analyses of Hsp104 (Wendler et al., 2007). Superposition of each GASBOR solution for Hsp104 and Hsp104$^{\Delta N}$ (Figures S2B and S2C) revealed consensus that was confirmed by the normalized spatial discrepancy (NSD) between independent calculations. NSD indicates the degree of discrepancy between the same relative position between any two structures (Volkov and Svergun, 2003). NSD values indicated little deviation between independent calculations, and reconstructions from different synchrotron trips yielded similar results (Figures 4E–4G; Table S2).

The outputs of each GASBOR calculation were averaged to provide filtered and unfiltered densities using DAMAVER (Figures 4E–4G) (Volkov and Svergun, 2003). Hsp104 shape reconstructions were oriented using Hsp104$^{\Delta N}$ hexamers, which when overlaid indicated where density for the missing NTD would fit (Figure 4F). The general dimensions of Hsp104 and Hsp104$^{\Delta N}$ particles determined by SAXS agree with Hsp104^{N728A} and Hsp104$^{\Delta N}$ cryo-EM reconstructions (Wendler et al., 2007), and the central channel through which substrate is translocated is resolved (Figures 4E–4G). Thus, we can identify conformational changes that enable Hsp104 and Hsp104$^{\Delta N}$ to couple ATPase activity to protein disaggregation.

Hsp104 and Hsp104$^{\Delta N}$ hexamers undergo large conformational changes between nucleotide states (Figures 4E–4G). Hsp104 and Hsp104$^{\Delta N}$ hexamers have similar width, but Hsp104$^{\Delta N}$ is shorter in height (Figures 4E and 4G). Two distinctive features change in each nucleotide state: (1) the placement of a projection of density on the hexamer exterior, along the plane of the largest dimension; and (2) the diameter and contours of the central channel (Figures 4E–4G, 5A, and 5B). The exterior projection is evident in the P(r) as a small population of large vectors that start around 175 Å (Figures 4C and 4D). Hsp104 and Hsp104$^{\Delta N}$ have dynamic projections that shift from a more

(B) R_g of Hsp104 and Hsp104$^{\Delta N}$ with the indicated nucleotide calculated by GNOM. These values closely match the Guinier approximations for R_g (Table S2). Values represent means ± SEM (n = 3–7).

(C and D) Real-space shape information for Hsp104 and Hsp104$^{\Delta N}$. Normalized P(r) curves (density distribution plots) generated by GNOM for Hsp104 (C) and Hsp104$^{\Delta N}$ (D) in the presence of AMP-PNP, ATPγS, ATP, ADP-AlF$_x$, ADP, and no nucleotide. P(r) plots are normalized to the area under the curve and overlaid to show differences between nucleotide states. Insets display the P(r) peak, which reveals differences between nucleotide states. Compared to Hsp104, Hsp104$^{\Delta N}$ has large spatial extent in the absence of nucleotide relative to its nucleotide-bound states.

(E–G) Averaged ab initio GASBOR volume reconstructions of Hsp104 (E) and Hsp104$^{\Delta N}$ (G). Filtered density is solid blue (Hsp104) or orange (Hsp104$^{\Delta N}$) overlaid with the unfiltered average shown in gray mesh. NSD of averaged models and q range used for reconstructions are shown plus average particle dimensions. (F) Overlay of Hsp104 and Hsp104$^{\Delta N}$ average reconstructions for each state, which was used to orient particles. Reconstructions are oriented with the N terminus pointing toward the top of the page.

See also Tables S2 and S3, Figure S2, Movie S1, and Movie S2.

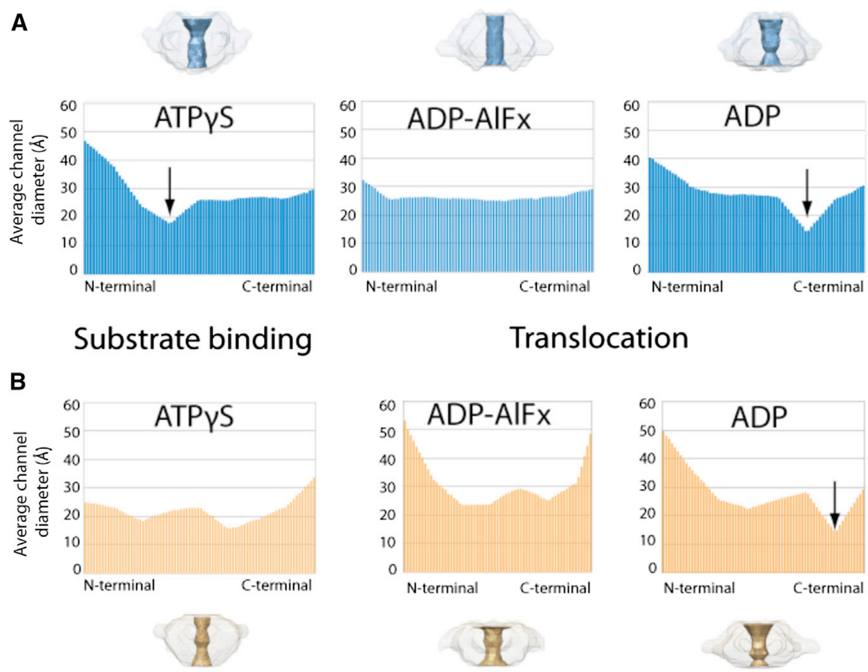

Figure 5. Channel Motions of Hsp104 and Hsp104$^{\Delta N}$ Hexamers

(A and B) Cut-away side views of Hsp104 (A) and Hsp104$^{\Delta N}$ (B) hexamers in ATPγS, ADP-AlF$_x$, or ADP. The channel was reconstructed using the filtered average volumes for each nucleotide state. Bar graphs display the average channel diameter (Å) of each z slice starting from the N terminus. Each bar represents 1 Å, and the number of bars represents the length of the channel that is closed for 360°. Substrate binds in the ATPγS state and is translocated from the N-terminal entrance to the C-terminal exit. The Hsp104 channel exhibits a peristaltic wave motion: dilation at the N-terminal entrance (in ATPγS) followed by a contraction of the N-terminal end of the channel (in ADP-AlF$_x$) and finally a shift in the location of a constriction from the N- to the C-terminal region (in ADP, arrow). The Hsp104$^{\Delta N}$ hexamer displays defects in the peristalsis motion, especially at the N-terminal channel entrance, which fails to contract in the ADP-AlF$_x$ and ADP states.
See also Movie S1 and Movie S2.

N-terminal position (in no nucleotide, AMP-PNP, ATPγS, and ATP) to a more C-terminal position (in ADP-AlF$_x$ and ADP) upon ATP hydrolysis (Figures 4E–4G, 5A, and 5B; Movie S1 and Movie S2). Rudimentary rigid body domain fitting reveals that the volumetric envelopes readily accommodate six Hsp104 monomers (Figure S2D). The external projection is likely the MD in accord with cryo-EM models of HAP plus ATPγS and ClpP (Figure S2D) (Carroni et al., 2014). Thus, our SAXS reconstructions resolve controversy surrounding MD location generated by cryo-EM studies (Lee et al., 2010; Wendler et al., 2007, 2009). The change in position of the external projection (Figures 4E–4G) is consistent with the MD located on the surface of the hexamer, which can move from an N-terminal, horizontal position to a C-terminally tilted position (Carroni et al., 2014; DeSantis et al., 2014).

To disaggregate substrates, Hsp104 translocates proteins through its central channel. Thus, we focused on the central channel (Figures 5A and 5B). The changes in shape of the Hsp104 channel are reminiscent of a peristaltic wave: there is dilation at the site of substrate entrance followed by a wave of constriction that travels in the direction that substrate is being pumped. Substrate enters through the N-terminal entrance and can be expelled from the C-terminal exit (Shorter, 2008). Accordingly, in the ATPγS state where Hsp104 initially engages substrate, the N-terminal channel entrance of Hsp104 is open and dilated with a diameter of ~45–50 Å (Figure 5A). In the ATPγS state, there is a region of constriction (channel diameter ~18 Å) after the N-terminal opening (Figure 5A, arrow), and C-terminal to this constriction the channel is ~25–30 Å in diameter. The channel constricts to a diameter of ~25–30 Å across its entire length with the transition state mimic ADP-AlF$_x$ (Figure 5A), the state with the smallest R_g (Figure 4B). Thus, upon ATP hydrolysis the Hsp104 channel constricts (Figure 5A). In the ADP state, a C-terminal point of constriction becomes apparent (Figure 5A, arrow), which likely helps expel substrate from the C-terminal exit. Thus, cycles of ATP binding and hydrolysis drive a peristaltic pumping motion of the Hsp104 hexamer, which likely drives directional substrate translocation (Movie S1). The peristaltic pumping motion likely underpins how Hsp104 transduces energy from ATP hydrolysis to conformational change and substrate remodeling using physical force.

NTD deletion grossly perturbs this peristaltic pump motion (Figure 5B; Movie S2). In ATPγS, the Hsp104$^{\Delta N}$ channel is narrow in diameter (~16–30 Å) compared to Hsp104, and there is no dilation at the N-terminal entrance (Figures 5A and 5B). Thus, it is more difficult for substrate to access the Hsp104$^{\Delta N}$ channel in the binding-competent ATPγS state. In ADP-AlF$_x$, the Hsp104$^{\Delta N}$ channel is dilated at N- and C-terminal ends, and only a central portion of the channel is ~25–30 Å in diameter, unlike Hsp104, where the channel aperture is ~25–30 Å across its whole length (Figures 5A and 5B). Thus, the "power stroke" motion elicited by ATP hydrolysis in Hsp104 is profoundly altered in Hsp104$^{\Delta N}$. In ADP, the Hsp104$^{\Delta N}$ and Hsp104 channels change in diameter in a similar manner along their length, although the N-terminal channel entrance is more dilated in Hsp104$^{\Delta N}$ (Figures 5A and 5B). The more dilated Hsp104$^{\Delta N}$ channel in ADP-AlF$_x$ might allow substrate to escape the channel. These channel defects help explain why Hsp104$^{\Delta N}$ is defective in translocation, unfolding, and disaggregation.

Hsp104$^{\Delta N}$ hexamers Operate Differently Than Hsp104 Hexamers

The profound alterations in the Hsp104$^{\Delta N}$ channel (Figures 4E–4G, 5A, and 5B) indicated that Hsp104$^{\Delta N}$ and Hsp104 might coordinate substrate translocation differently. Indeed, Hsp104$^{\Delta N}$ hexamers appear unable to process substrate in a subglobally

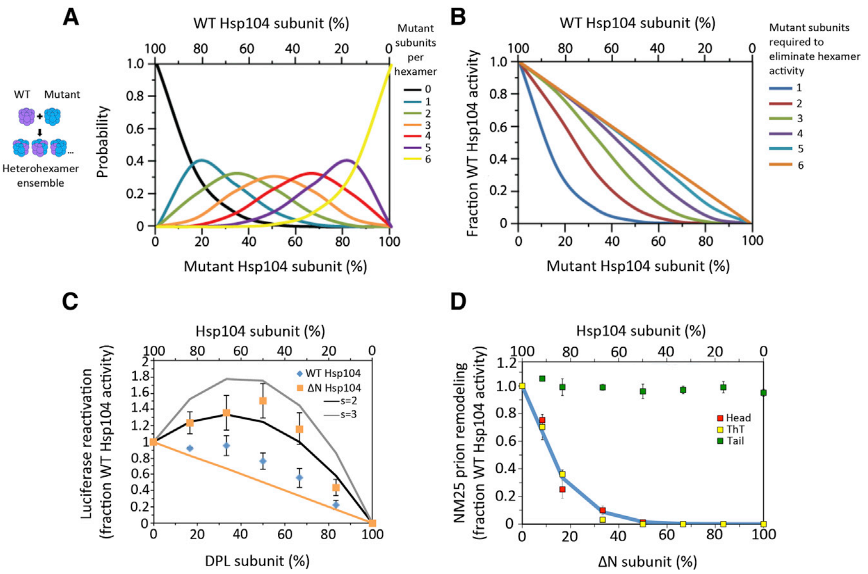

Figure 6. Altered Substrate Handling by Hsp104$^{\Delta N}$ Hexamers Precludes Prion Dissolution

(A) Theoretical Hsp104 hexamer ensembles containing zero (black), one (blue), two (green), three (orange), four (red), five (purple), and six (yellow) mutant subunits as a function of fraction mutant subunit.

(B) Theoretical activity curves where one or more (blue), two or more (red), three or more (green), four or more (purple), five or more (light blue), or six mutant subunits (orange) ablate Hsp104 hexamer activity.

(C) Luciferase aggregates were treated with Hsp104 (blue markers) or Hsp104$^{\Delta N}$ (orange markers), Hsp72, and Hdj2 plus increasing fractions of Hsp104^{DPL} (blue markers) or Hsp104$^{\Delta NDPL}$ (orange markers) subunits. Luciferase reactivation was determined (fraction WT Hsp104 activity). Values represent means ± SEM (n = 3–4). Theoretical disaggregase activity if six DPL subunits ablate hexamer activity (orange line). Theoretical curves are shown wherein adjacent pairs of WT:WT (or ΔN:ΔN) or WT:DPL (or ΔN:ΔNDPL) subunits confer hexamer activity, while adjacent DPL (or ΔNDPL) subunits have no activity. Each adjacent WT:WT (or ΔN:ΔN) pair has an activity of 1/6. Adjacent WT:DPL (or ΔN:ΔNDPL) pairs have a stimulated activity (s), and the effect of s = 2 (black curve) or s = 3 (gray curve) is shown.

(D) NM25 prions were treated with Hsp104, Sse1, Ssa1, and Sis1 plus increasing fractions of Hsp104$^{\Delta N}$. Remodeling was monitored by Head contact integrity (for G31C-pyrene-labeled NM25 prions, red markers), ThT fluorescence (for unlabeled NM25 prions, yellow markers), or Tail contact integrity (for G96C-pyrene-labeled NM25 prions, green markers). Values represent means ± SEM (n = 3). Theoretical disaggregase activity if 1 Hsp104$^{\Delta N}$ subunit ablates hexamer activity (blue line).

See also Figure S1.

or globally cooperative manner required for prion dissolution (DeSantis et al., 2012). We utilized a mutant subunit doping strategy to generate heterohexamer ensembles and determine whether subunit collaboration was altered with respect to substrate handling in Hsp104$^{\Delta N}$ (Figures 6A and 6B) (DeSantis et al., 2012).

To define how Hsp104$^{\Delta N}$ subunits coordinate substrate binding during disordered aggregate dissolution, we employed the "double pore loop" (DPL, Y257A:Y662A) mutant. DPL has normal ATPase activity but harbors Y257A and Y662A mutations in substrate-binding pore loops, which impair substrate translocation (DeSantis et al., 2012). We assembled heterohexamer ensembles of Hsp104 and Hsp104^{DPL}, or Hsp104$^{\Delta N}$ and Hsp104$^{\Delta NDPL}$, and assessed disaggregase activity against disordered luciferase aggregates. Hsp104 and Hsp104$^{\Delta N}$ hexamers responded very differently to DPL subunits (Figure 6C). Hsp104^{DPL} subunits caused a roughly linear decline in Hsp104 luciferase reactivation activity, indicating probabilistic substrate handling (Figure 6C) (DeSantis et al., 2012). By contrast, Hsp104$^{\Delta NDPL}$ subunits stimulated Hsp104$^{\Delta N}$ activity and only inhibited when the average number of Hsp104$^{\Delta NDPL}$ subunits per hexamer exceeded 4 (Figure 6C). We could model this behavior if we imposed rules whereby an Hsp104$^{\Delta NDPL}$ subunit stimulates the activity of an adjacent Hsp104$^{\Delta N}$ subunit by ~2-fold but exerts an inhibitory effect if it is adjacent to a mutant subunit (Figure 6C) (DeSantis et al., 2012). Thus, Hsp104$^{\Delta N}$ subunits cooperate negatively with respect to substrate binding. Addition of up to 4 substrate-binding defective subunits within the Hsp104$^{\Delta N}$ hexamer stimulates activity against disordered aggregates. Thus, the NTD is essential for cooperative substrate handling by the Hsp104 hexamer.

Hsp104$^{\Delta N}$ Subunits Inhibit Prion Dissolution by Hsp104 Hexamers

The negative cooperativity of Hsp104$^{\Delta N}$ subunits with respect to substrate binding likely precludes prion dissolution by Hsp104$^{\Delta N}$, which requires multiple subunits within the hexamer to work together (DeSantis et al., 2012). To assess how Hsp104$^{\Delta N}$ subunits affected prion remodeling by Hsp104, we doped Hsp104$^{\Delta N}$ subunits into Hsp104 hexamers and assessed ability to (1) break Head and Tail prion contacts, and (2) dissolve NM25 prions (NM prions formed at 25°C). Tail contact severing was unaffected by Hsp104$^{\Delta N}$ subunits, whereas a single Hsp104$^{\Delta N}$ subunit per Hsp104 hexamer inhibited Head contact severing and elimination of amyloid structure (Figure 6D). Thus, all six Hsp104 subunits must possess the NTD for globally cooperative prion dissolution.

Hsp104$^{\Delta N}$ Is Not Potentiated by Mutations in the MD

Hsp104 disaggregase activity is potentiated by specific mutations in the MD, which enable Hsp104 to dissolve TDP-43, FUS, and α-syn fibrils and mitigate neurodegeneration under conditions where Hsp104 is inactive (Jackrel et al., 2014). We tested whether potentiating MD mutations, A503S and A503V, could overcome defects in cooperativity caused by NTD deletion. Unlike their full-length counterparts, Hsp104$^{\Delta N\text{-}A503V}$ and Hsp104$^{\Delta N\text{-}A503S}$ could not rescue TDP-43, FUS, or α-syn toxicity in yeast, despite robust expression (Figures 7A and 7B). Moreover, Hsp104$^{\Delta N\text{-}A503V}$ and Hsp104$^{\Delta N\text{-}A503S}$ failed to rescue α-syn or FUS aggregation in yeast, unlike Hsp104^{A503V} (Figures 7C–7F). Thus, the NTD is essential for potentiation of the Hsp104 hexamer by specific MD mutations.

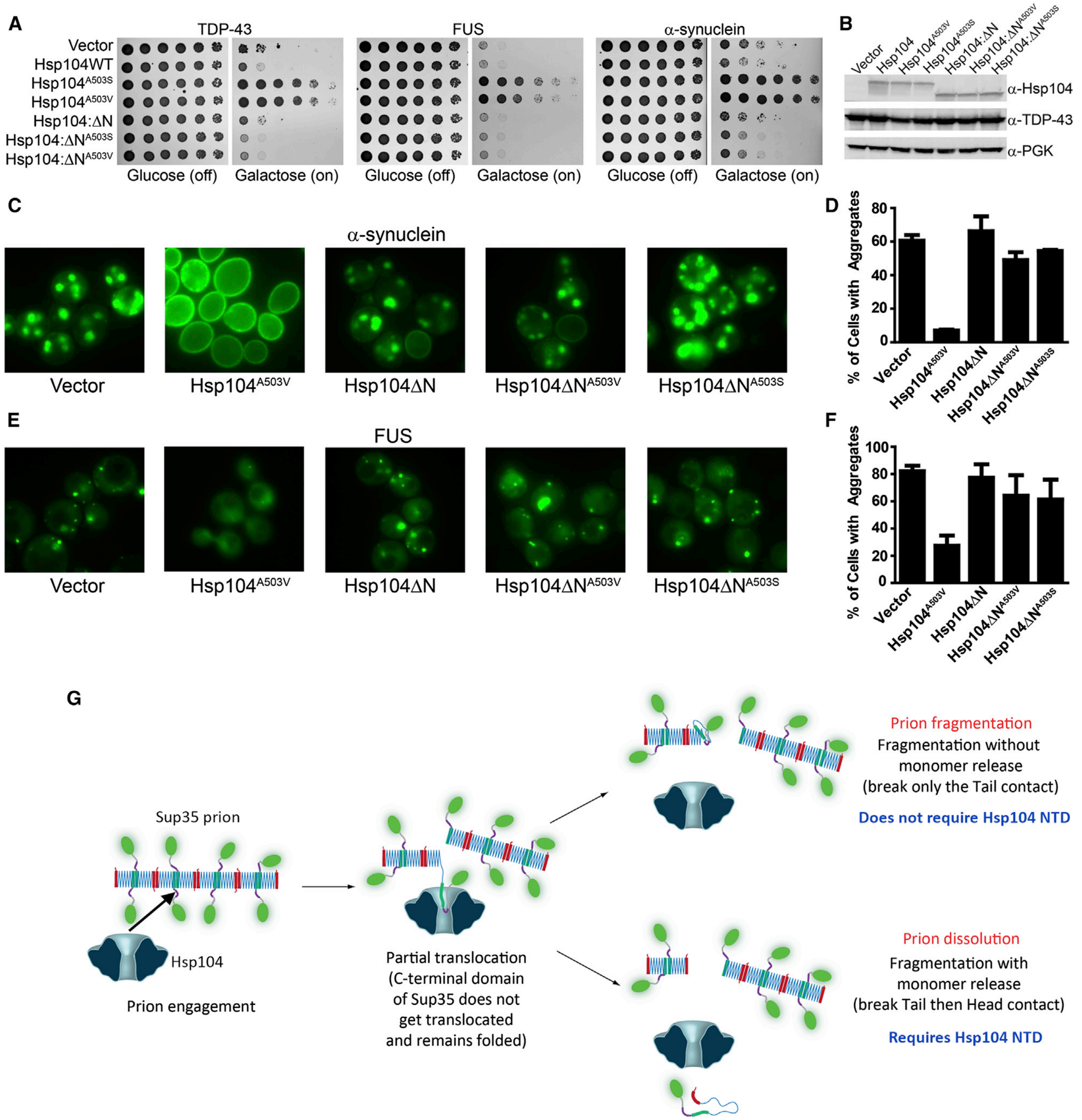

Figure 7. Deletion of the Hsp104 NTD Inhibits Hsp104 Potentiation

(A) Δ*hsp104* yeast integrated with galactose-inducible TDP-43, FUS, or α-syn was transformed with the indicated Hsp104 variant or vector. Strains were serially diluted 5-fold and spotted on glucose (off) or galactose (on) media.

(B) Selected yeast from (A) were induced for 5 hr, lysed, and immunoblotted. 3-phosphoglycerate kinase (PGK) serves as a loading control.

(C) Fluorescence microscopy of cells expressing α-syn-YFP plus indicated Hsp104 variant or vector.

(D) Quantification of α-syn aggregation. Values represent means ± SEM (n = 2).

(E) Fluorescence microscopy of cells expressing FUS-GFP plus indicated Hsp104 variant or vector.

(F) Quantification of FUS aggregation. Values represent means ± SEM (n = 2).

(G) Model of Sup35 prion fragmentation versus dissolution by Hsp104. Hsp104 initially engages Sup35 prions in a region (residues 96–151; purple) C-terminal to the Tail contact (dark green). Directional pulling on N-terminal cross-β structure leads to partial translocation and breakage of the Tail contact and Sup35 prion fragmentation. Further translocation breaks Central Core contacts (blue) and the Head contacts (red), resulting in monomer release. Thus, Sup35 prions are fragmented with or without monomer release. The Sup35 C-terminal domain remains folded throughout. $Hsp104^{\Delta N}$ can break the Tail but not the Central Core or Head contacts, thus fragmenting Sup35 prions without solubilizing Sup35.

DISCUSSION

We have established that the Hsp104 NTD is essential for nucleotide-dependent conformational changes that enable productive hexamer cooperativity, plasticity, and potentiation. Reconstruction of Hsp104 hexamers in solution via SAXS revealed conformational changes that drive a peristaltic pumping motion triggered by ATP hydrolysis and completed by release of Pi. This peristaltic pumping motion likely drives directional substrate translocation through the N-terminal channel entrance, across the central channel, and out the C-terminal exit, but is grossly perturbed in Hsp104$^{\Delta N}$.

Mutant doping revealed negative cooperativity between substrate-binding pore loops in Hsp104$^{\Delta N}$ hexamers. Remarkably, Hsp104$^{\Delta N}$ hexamers containing ~1–4 subunits that cannot engage substrate outperform Hsp104$^{\Delta N}$ hexamers in disaggregation of disordered aggregates. Thus, the NTD regulates substrate binding and prevents nonproductive competition for substrate binding by pore loops. This finding helps explain why Hsp104$^{\Delta N}$ is less active than Hsp104 in disaggregating disordered aggregates. Although subunit cooperativity is not essential for disordered aggregate dissolution (DeSantis et al., 2012), it is necessary for optimal activity and adaptable hexamer function. This deficiency in Hsp104$^{\Delta N}$ hexamer cooperativity due to defects in conformational changes results in deregulated ATPase activity, reduced disaggregase, unfoldase, and translocase activity, and an inability to dissolve stable amyloid, even in the presence of potentiating mutations. Hsp104$^{\Delta N}$ is slightly less able to collaborate with Hsp70 and Hsp40 (Figure 1D), which might also contribute to reduced amyloid dissolution. However, amyloid dissolution by Hsp104 does not typically require Hsp70 and Hsp40 (DeSantis et al., 2012); thus we suggest that altered subunit cooperativity is the major defect limiting amyloid dissolution by Hsp104$^{\Delta N}$.

Cryo-EM reconstructions of Hsp104 have fueled controversy, and a clear picture of how Hsp104 drives protein disaggregation has not emerged from these studies. Controversy has been compounded by the use of only dysfunctional Hsp104 mutants in a limited number of nucleotide states: only ATPγS, ATP, and ADP have been explored (Carroni et al., 2014; Lee et al., 2010; Wendler et al., 2007, 2009). It is difficult to relate these findings to WT Hsp104. To provide an independent view, we employed SAXS, a powerful method to study structural changes of AAA+ proteins in solution (Chen et al., 2010). SAXS is performed in solution, under conditions where Hsp104 is active, eliminating issues caused by freezing or fixation in cryo-EM. We reconstructed Hsp104 and Hsp104$^{\Delta N}$ in AMP-PNP, ATPγS, ATP, ADP-AlF$_x$ (hydrolysis transition state), ADP, and apo states to a nominal resolution of 7.6–8.4 Å. Thus, we provide the highest-resolution and most comprehensive set of volume envelopes for Hsp104 (which has not been studied by cryo-EM) and Hsp104$^{\Delta N}$ hexamers to date. By studying Hsp104 in various nucleotides, we uncover hexameric states that are likely populated during its natural ATPase cycle. We revealed a peristaltic pumping motion of the central channel that drives directional substrate translocation, which is profoundly altered in Hsp104$^{\Delta N}$. This finding helps explain several functional deficits of Hsp104$^{\Delta N}$. However, pore shape is unlikely to be the only determinant of substrate translocation, and it is critical to define the location of the substrate-binding pore loops in each nucleotide state. Future studies will fit atomic models of Hsp104 monomers into these SAXS envelopes and will be constrained by X-ray footprinting data (DeSantis et al., 2014).

We have elucidated the mechanism of Sup35 prion severing and dissolution by Hsp104. Hsp104 engages Sup35 prions by binding to a region spanning amino acids 96–151 (Figure 7G, purple regions). Hsp104 then exerts a directional pulling force that selectively unfolds cross-β structure N-terminal to this binding site, but does not unfold domains C-terminal to this binding site (Figure 7G). This partial translocation mechanism enables Hsp104 to dissolve Sup35 prions without unfolding the C-terminal GTPase domain (Figure 7G). Thus, Hsp104 rapidly releases functional, folded protein from the prion to rapidly cure the loss-of-function [*PSI*$^+$] phenotype (Paushkin et al., 1996).

After engaging the prion, Hsp104 resolves cross-β structure N-terminal to its binding site in three steps: (1) the Tail-to-Tail contact is broken (Figure 7G, dark green regions), (2) the central cross-β core is unfolded (Figure 7G, blue regions), and (3) the Head-to-Head contact is broken to release soluble Sup35 (Figure 7G, red regions). This sequence was confirmed by covalently stapling the Tail-to-Tail or Head-to-Head contact with BMB. Thus, Hsp104 severed prions with a covalent Head-to-Head contact by breaking the Tail-to-Tail contact, but could not fragment prions with a covalent Tail-to-Tail contact.

Hsp104$^{\Delta N}$ is specifically defective in the second and third steps of this process. Hsp104$^{\Delta N}$ engages the same binding site on Sup35 prions and breaks the Tail-to-Tail contact. However, Hsp104$^{\Delta N}$ is unable to unfold the central core or break the Head-to-Head contact. Thus, Hsp104$^{\Delta N}$ is capable of fragmenting but not dissolving Sup35 prions (Figure 7G). The ability of Hsp104$^{\Delta N}$ to fragment but not dissolve Sup35 prions explains why it can propagate [*PSI*$^+$], but not readily eliminate it at high concentrations in vivo (Hung and Masison, 2006). Indeed, in vitro, Hsp104$^{\Delta N}$ operates in a way that only stimulates Sup35 prionogenesis and selectively amplifies strong [*PSI*$^+$] prions.

Curiously, Hsp104$^{\Delta N}$ overexpression very slowly cures [*PSI*$^+$] in some genetic backgrounds but not others (Park et al., 2014). It was proposed that Hsp104$^{\Delta N}$ promotes Sup35 prion dissolution via a "trimming" activity that solubilizes Sup35 only from the ends of prion fibrils (Park et al., 2014). Our findings provide a rationale for this proposed activity. Selective cleavage of the Tail-to-Tail contact by Hsp104$^{\Delta N}$ could liberate soluble Sup35 at the subset of fibril ends where the Tail-to-Tail contact holds the final monomer to the fibril. However, we did not observe dissolution of Sup35 from assembled prions by Hsp104$^{\Delta N}$ in vitro. Released monomers could be rapidly converted to the prion form by fibril ends or Hsp104$^{\Delta N}$ may not access fibril ends in vitro. In vivo, other factors not reconstituted here might prevent this reassociation or selectively target Hsp104$^{\Delta N}$ to Sup35 prion fibril ends.

Mechanisms distinct from prion dissolution have been proposed to explain [*PSI*$^+$] curing by Hsp104 overexpression including inhibition of Sup35 prion fragmentation (Winkler et al., 2012). Based on colocalization studies, it was proposed that the Hsp104 NTD mediated binding to large NM-YFP aggregates and displaced Ssa1, thereby perturbing prion fragmentation (Winkler et al., 2012). However, overexpression of the Hsp104 NTD alone does not cure [*PSI*$^+$] (Hung and Masison, 2006). It is unclear whether the colocalization reflects direct binding, as Hsp104 and Hsp104$^{\Delta N}$ bind pure Sup35 prions with similar affinity. Moreover, these results are uncorroborated with native untagged proteins, and large NM-YFP aggregates are not disseminated prions. Importantly, [*PSI*$^+$] curing kinetics by Hsp104 overexpression are inconsistent with inhibition of prion fragmentation (Park et al., 2014). This mechanism also fails to explain why Hsp104$^{\Delta N}$ cures [*PSI*$^+$] in some genetic backgrounds (Park et al., 2014).

We have established that the NTD is essential for potentiation of Hsp104 activity by specific MD mutations. Unlike their full-length counterparts, neither Hsp104$^{\Delta N\text{-}A503V}$ nor Hsp104$^{\Delta N\text{-}A503S}$ rescued TDP-43, FUS, or α-syn toxicity in yeast. Potentiating mutations at the A503 position of the MD likely promote an allosteric activation step that enhances Hsp104 ATPase, unfoldase, and disaggregase activity (Jackrel et al., 2014). These effects are ablated by NTD deletion. We conclude that optimal Hsp104 functionality depends on the NTD, which enables hexamer plasticity and potentiation.

EXPERIMENTAL PROCEDURES

Proteins

Proteins were purified using standard protocols. For more details, see Supplemental Experimental Procedures.

Size-Exclusion Chromatography

Absolute molecular weights of apo hexamers of Hsp104 and Hsp104$^{\Delta N}$ (15 μM monomer) were determined using multiangle light scattering coupled with refractive interferometric detection and a TSK4000 size-exclusion column.

NTPase Activity

Hsp104 ATPase and Sup35 GTPase activity was assessed as described (DeSantis et al., 2012; Krzewska et al., 2007).

Protein Disaggregation

Luciferase disaggregation and reactivation in vitro and in vivo were as described (DeSantis et al., 2012). Amyloid and prion disaggregation was as described (DeSantis et al., 2012). For more details, see Supplemental Experimental Procedures.

Thermotolerance

Yeast thermotolerance was assessed as described (DeSantis et al., 2012).

Sup35 Prionogenesis and Transformation

Sup35 prionogenesis in vitro and transformation were performed as described (DeSantis and Shorter, 2012; Shorter and Lindquist, 2006). For more details, see Supplemental Experimental Procedures.

Site-Resolved Pyrene and Acrylodan Fluorescence

Pyrene and acrylodan fluorescence were monitored as described (Krishnan and Lindquist, 2005).

Site-Resolved BPMTS Crosslinking

Single cysteine NM variants (10 μM) bearing BPMTS at the indicated position were assembled into prions with agitation at 1,400 rpm (Eppendorf thermomixer) in the dark. Crosslinking was elicited by UV irradiation at 365 nm for 20 min. Samples were processed for reducing SDS-PAGE and immunoblot. For more details, see Supplemental Experimental Procedures.

SAXS/WAXS

X-ray scattering data were collected at beamline 4-2 at Stanford Synchrotron Radiation Laboratory (SSRL, Menlo Park, CA) and beamline X9 at the National Synchrotron Light Source (NSLS, Upton, NY). Data were collected and analyzed as described (DeSantis et al., 2014). Shape reconstructions of the hexamer were generated using GASBOR (Svergun et al., 2001). Six-fold symmetry was imposed. Reconstructions were averaged and filtered using DAMAVER and converted to volume envelopes using SITUS (Volkov and Svergun, 2003; Wriggers et al., 1999). For more details, see Supplemental Experimental Procedures.

Mutant Doping Studies

Mathematical modeling and mutant doping studies were as described (DeSantis et al., 2012).

Yeast Proteinopathy Models

Yeast strains integrated with galactose-inducible TDP-43, FUS, or α-syn were transformed with the indicated galactose-inducible Hsp104 variant or vector. Toxicity, aggregation, and expression were assessed as described (Jackrel et al., 2014).

ACCESSION NUMBERS

The SAXS data have been deposited in BIOISIS, an open-access database dedicated to the study of biological macromolecules by SAXS (http://www.bioisis.net/). The accession codes are available upon request from the authors.

SUPPLEMENTAL INFORMATION

Supplemental Information includes two figures, three tables, two movies, and Supplemental Experimental Procedures and can be found with this article at http://dx.doi.org/10.1016/j.molcel.2014.12.021.

ACKNOWLEDGMENTS

We thank Sue Lindquist, Walid Houry, Aaron Gitler, Martin Duennwald, and Laura Castellano for kindly providing reagents; Marta Carroni and Helen Saibil for sharing HAP model coordinates; Greg Van Duyne for help with SAXS; and Hiro Tsuruta, Lin Yang, and Marc Allaire for beamline assistance. This work was funded by American Heart Association predoctoral (E.A.S.) and postdoctoral (M.E.J.) fellowships; NIH grants T32GM008275 (E.A.S. and M.A.S.), T32GM071339 (M.E.D.), F31NS079009 (M.E.D.), DP2OD002177 (J.S.), and R01GM099836 (J.S.); an Ellison Medical Foundation New Scholar in Aging Award, Target ALS, Muscular Dystrophy Association (MDA277268), and The Robert Packard Center for ALS Research at Johns Hopkins University (J.S.).

Received: August 26, 2014
Revised: November 6, 2014
Accepted: December 12, 2014
Published: January 22, 2015

REFERENCES

Barnett, M.E., Nagy, M., Kedzierska, S., and Zolkiewski, M. (2005). The amino-terminal domain of ClpB supports binding to strongly aggregated proteins. J. Biol. Chem. *280*, 34940–34945.

Carroni, M., Kummer, E., Oguchi, Y., Wendler, P., Clare, D.K., Sinning, I., Kopp, J., Mogk, A., Bukau, B., and Saibil, H.R. (2014). Head-to-tail interactions of the coiled-coil domains regulate ClpB activity and cooperation with Hsp70 in protein disaggregation. eLife *3*, e02481.

Chen, B., Sysoeva, T.A., Chowdhury, S., Guo, L., De Carlo, S., Hanson, J.A., Yang, H., and Nixon, B.T. (2010). Engagement of arginine finger to ATP triggers large conformational changes in NtrC1 AAA+ ATPase for remodeling bacterial RNA polymerase. Structure *18*, 1420–1430.

DeSantis, M.E., and Shorter, J. (2012). Hsp104 drives "protein-only" positive selection of Sup35 prion strains encoding strong [PSI(+)]. Chem. Biol. *19*, 1400–1410.

DeSantis, M.E., Leung, E.H., Sweeny, E.A., Jackrel, M.E., Cushman-Nick, M., Neuhaus-Follini, A., Vashist, S., Sochor, M.A., Knight, M.N., and Shorter, J. (2012). Operational plasticity enables hsp104 to disaggregate diverse amyloid and nonamyloid clients. Cell *151*, 778–793.

DeSantis, M.E., Sweeny, E.A., Snead, D., Leung, E.H., Go, M.S., Gupta, K., Wendler, P., and Shorter, J. (2014). Conserved distal loop residues in the Hsp104 and ClpB middle domain contact nucleotide-binding domain 2 and enable Hsp70-dependent protein disaggregation. J. Biol. Chem. *289*, 848–867.

Hung, G.C., and Masison, D.C. (2006). N-terminal domain of yeast Hsp104 chaperone is dispensable for thermotolerance and prion propagation but necessary for curing prions by Hsp104 overexpression. Genetics *173*, 611–620.

Jackrel, M.E., DeSantis, M.E., Martinez, B.A., Castellano, L.M., Stewart, R.M., Caldwell, K.A., Caldwell, G.A., and Shorter, J. (2014). Potentiated Hsp104 variants antagonize diverse proteotoxic misfolding events. Cell *156*, 170–182.

Krishnan, R., and Lindquist, S.L. (2005). Structural insights into a yeast prion illuminate nucleation and strain diversity. Nature *435*, 765–772.

Krzewska, J., Tanaka, M., Burston, S.G., and Melki, R. (2007). Biochemical and functional analysis of the assembly of full-length Sup35p and its prion-forming domain. J. Biol. Chem. *282*, 1679–1686.

Lee, S., Sielaff, B., Lee, J., and Tsai, F.T. (2010). CryoEM structure of Hsp104 and its mechanistic implication for protein disaggregation. Proc. Natl. Acad. Sci. USA *107*, 8135–8140.

Lum, R., Niggemann, M., and Glover, J.R. (2008). Peptide and protein binding in the axial channel of Hsp104. Insights into the mechanism of protein unfolding. J. Biol. Chem. *283*, 30139–30150.

Park, Y.N., Zhao, X., Yim, Y.I., Todor, H., Ellerbrock, R., Reidy, M., Eisenberg, E., Masison, D.C., and Greene, L.E. (2014). Hsp104 overexpression cures *Saccharomyces cerevisiae* [*PSI*$^+$] by causing dissolution of the prion seeds. Eukaryot. Cell *13*, 635–647.

Paushkin, S.V., Kushnirov, V.V., Smirnov, V.N., and Ter-Avanesyan, M.D. (1996). Propagation of the yeast prion-like [*psi*$^+$] determinant is mediated by oligomerization of the SUP35-encoded polypeptide chain release factor. EMBO J. *15*, 3127–3134.

Shorter, J. (2008). Hsp104: a weapon to combat diverse neurodegenerative disorders. Neurosignals *16*, 63–74.

Shorter, J., and Lindquist, S. (2006). Destruction or potentiation of different prions catalyzed by similar Hsp104 remodeling activities. Mol. Cell *23*, 425–438.

Svergun, D.I. (1992). Determination of the Regularization Parameter in Indirect-Transform Methods Using Perceptual Criteria. J. Appl. Cryst. *25*, 495–503.

Svergun, D.I., Petoukhov, M.V., and Koch, M.H. (2001). Determination of domain structure of proteins from X-ray solution scattering. Biophys. J. *80*, 2946–2953.

Tipton, K.A., Verges, K.J., and Weissman, J.S. (2008). In vivo monitoring of the prion replication cycle reveals a critical role for Sis1 in delivering substrates to Hsp104. Mol. Cell *32*, 584–591.

Volkov, V.V., and Svergun, D.I. (2003). Uniqueness of ab initio shape determination in small-angle scattering. J. Appl. Cryst. *36*, 860–864.

Wendler, P., Shorter, J., Plisson, C., Cashikar, A.G., Lindquist, S., and Saibil, H.R. (2007). Atypical AAA+ subunit packing creates an expanded cavity for disaggregation by the protein-remodeling factor Hsp104. Cell *131*, 1366–1377.

Wendler, P., Shorter, J., Snead, D., Plisson, C., Clare, D.K., Lindquist, S., and Saibil, H.R. (2009). Motor mechanism for protein threading through Hsp104. Mol. Cell *34*, 81–92.

Winkler, J., Tyedmers, J., Bukau, B., and Mogk, A. (2012). Hsp70 targets Hsp100 chaperones to substrates for protein disaggregation and prion fragmentation. J. Cell Biol. *198*, 387–404.

Wriggers, W., Milligan, R.A., and McCammon, J.A. (1999). Situs: A package for docking crystal structures into low-resolution maps from electron microscopy. J. Struct. Biol. *125*, 185–195.

Molecular Cell, Volume *57*

Supplemental Information

The Hsp104 N-Terminal Domain Enables Disaggregase Plasticity and Potentiation

Elizabeth A. Sweeny, Meredith E. Jackrel, Michelle S. Go, Matthew A. Sochor, Beatrice M. Razzo, Morgan E. DeSantis, Kushol Gupta, and James Shorter

Fig. S1. Sweeny et al.

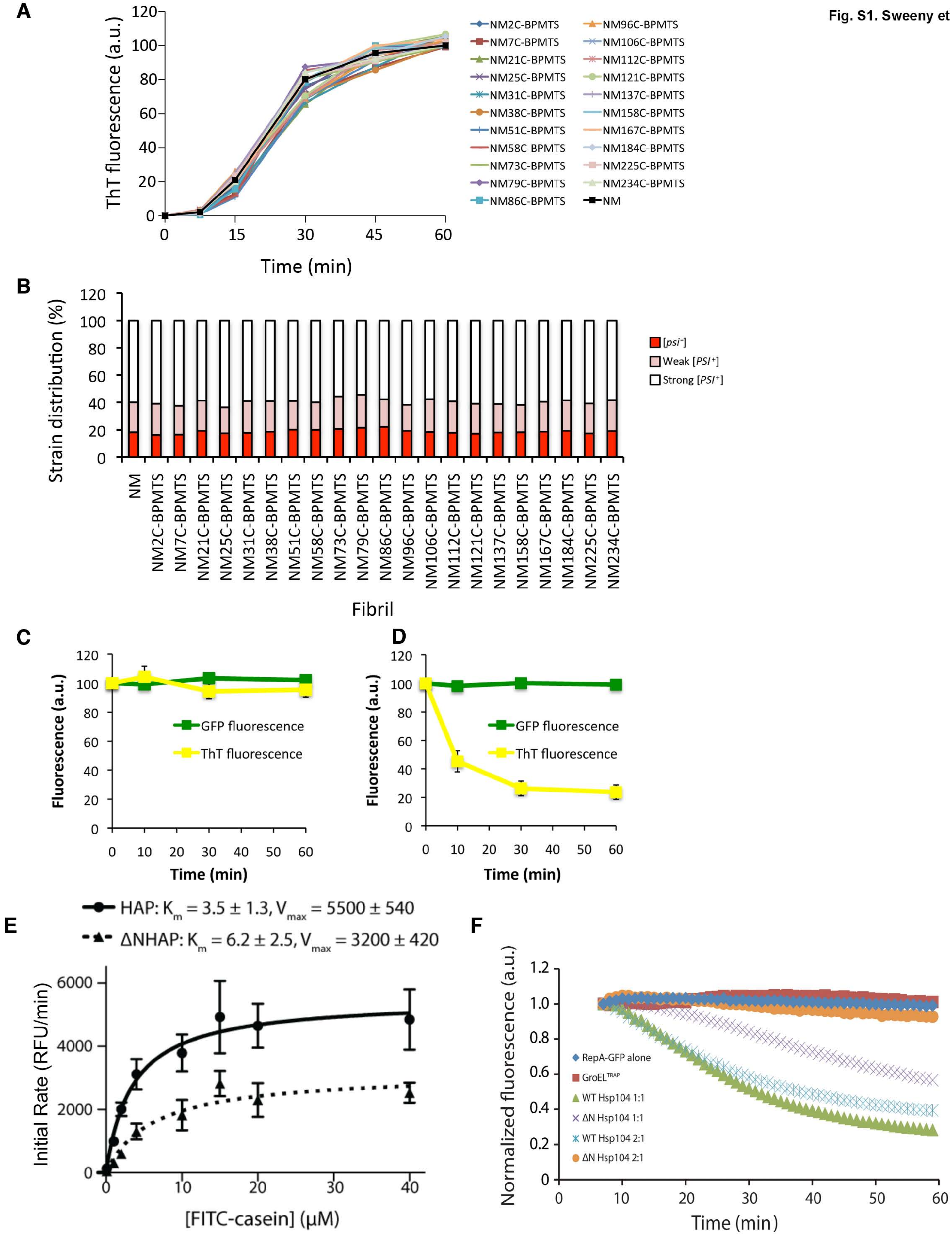

Figure S1. Hsp104$^{\Delta N}$ has impaired translocation and unfoldase activity. Related to Figure 3 and 6. (A) NM or BPMTS-labeled single cysteine NM variants (10μM) were agitated for 1h at 4°C. At the indicated times, prion assembly was assessed by ThT fluorescence. A representative dataset from three separate experiments in shown. **(B)** NM or BPMTS-labeled single cysteine NM variants were assembled into prions as in **(A)**. Reaction products were sonicated and transformed into [*psi*$^-$] cells. The proportion of [*psi*$^-$], weak [*PSI*$^+$], and strong [*PSI*$^+$] colonies was determined. A representative dataset from three separate experiments in shown. **(C, D)** NM lacks the C-terminal GTPase domain of Sup35 (amino acids 254-625; Figure 3D). Thus, does Hsp104 need to unfold domains C-terminal to NM to dissolve Sup35 prions? To answer this question, we employed NM-GFP, which forms prions in vivo (Tyedmers et al., 2010). NM-GFP retains similar GFP fluorescence in the prion and soluble state. Thus, GFP remains folded upon prionogenesis. To assess whether GFP was unfolded during Hsp104-catalzed prion dissolution we included $GroEL_{TRAP}$, which captures unfolded GFP and prevents refolding (Doyle et al., 2007). NM-GFP prions were treated with Hsp104$^{\Delta N}$ **(C)** or Hsp104 (1μM) **(D)** plus $GroEL_{TRAP}$, Sse1, Ssa1, and Sis1 for 0-1h. At various times, GFP fluorescence and ThT fluorescence was measured. Values represent means±SEM (n=3). As anticipated, treatment of NM-GFP prions with Hsp104$^{\Delta N}$ reduced neither GFP nor ThT fluorescence **(C)**. By contrast, Hsp104 disassembled NM-GFP prions as determined by ThT fluorescence **(D)**. However, GFP fluorescence was unchanged **(D)**, indicating that Hsp104 can disassemble NM-GFP prions without unfolding GFP. Thus, Hsp104 selectively resolves N-terminal prion structure without unfolding the appended C-terminal domain. **(E)** We determined K_m and V_{max} of FITC-casein degradation for HAP and HAP$^{\Delta N}$. HAP is an Hsp104 mutant (739-GSK-741 to 739-IGF-741) that translocates substrates into a chambered protease, ClpP (Tessarz et al., 2008). FITC is released and fluorescence increases upon FITC-casein translocation by HAP and subsequent degradation by ClpP. Increasing concentrations of FITC-casein were incubated with ClpP plus HAP or HAP$^{\Delta N}$. Degradation rates were plotted against FITC-casein concentration to determine K_{m} and V_{max}. Values represent means±SEM (n=3). HAP or HAP$^{\Delta N}$ K_{m} and V_{max} values are significantly different as determined by a two-tailed t-test ($p<0.05$). Compared to HAP, HAP$^{\Delta N}$ displayed an increased K_m as well as a reduced V_{max}, revealing defects in protein translocation. **(F)** To determine whether Hsp104$^{\Delta N}$ is a defective unfoldase, we used a RepA$_{1-70}$-GFP substrate. Here, the first seventy amino acids of RepA are appended to GFP and serve as a recognition signal for Hsp104 (Doyle et al., 2007). To track RepA$_{1-70}$-GFP unfolding by Hsp104 or Hsp104$^{\Delta N}$ in the absence of subsequent refolding, we added GroEL$_{TRAP}$ (Doyle et al., 2007). RepA$_{1-70}$-GFP was incubated with Hsp104 or Hsp104$^{\Delta N}$ and GroEL$_{TRAP}$ plus ATP:ATPγS (2:1 or 1:1). GFP unfolding was measured by fluorescence. A representative dataset from three separate experiments is shown. With 1:1 or 2:1 ATP:ATPγS, Hsp104 robustly unfolds RepA$_{1-70}$-GFP. By contrast, Hsp104$^{\Delta N}$ displayed reduced RepA$_{1-70}$-GFP unfoldase activity at 1:1 ATP:ATPγS, and was unable to unfold RepA$_{1-70}$-GFP at 2:1 ATP:ATPγS. Thus, Hsp104$^{\Delta N}$ is defective in substrate translocation and unfolding.

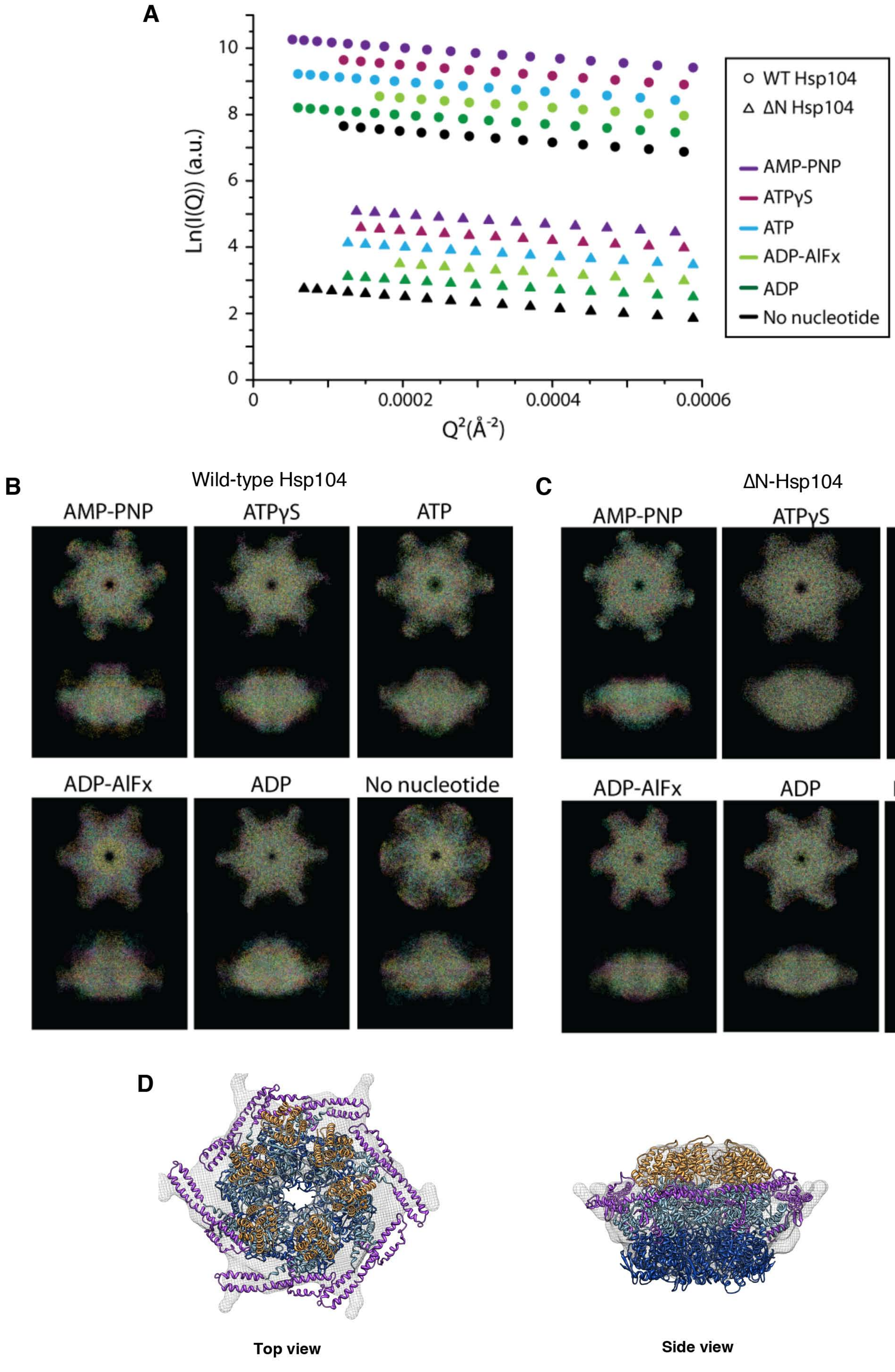
A
Ln(I(Q)) (a.u.)
Q^2(Å^{-2})
0
2
4
6
8
10
0
0.0002
0.0004
0.0006
WT Hsp104
ΔN Hsp104
AMP-PNP
ATPγS
ATP
ADP-AlFx
ADP
No nucleotide
B
Wild-type Hsp104
AMP-PNP
ATPγS
ATP
ADP-AlFx
ADP
No nucleotide
C
ΔN-Hsp104
AMP-PNP
ATPγS
ATP
ADP-AlFx
ADP
No nucleotide
D
Top view
Side view

Figure S2. Guinier analysis, GASBOR replicates, and rigid-body fitting individual Hsp104 domains into volume envelope generated from SAXS data. Related to Figure 4 and 5. (A) Guinier plots of the raw scattering for Hsp104 and Hsp104$^{\Delta N}$. Guinier plots of the raw scattering for Hsp104 and Hsp104$^{\Delta N}$ in the presence of AMP-PNP, ATPγS, ATP, ADP-AlF$_x$, ADP, and no nucleotide. Linearity of the Guinier plot indicates that there were no interparticle interactions such as aggregation. **(B, C)** GASBOR replicates. Each GASBOR (Svergun et al., 2001) model of Hsp104 **(B)** and Hsp104$^{\Delta N}$ **(C)** are overlaid to show agreement of the individual GASBOR solutions for each of the nucleotide states: AMP-PNP, ATPγS, ATP, ADP-AlF$_x$, ADP, and no nucleotide. **(D)** Rigid-body fitting individual Hsp104 domains into the volume envelope generated from SAXS/WAXS data of the Hsp104 hexamer in the presence of ATP. Individual Hsp104 domains were homology modeled based on the ClpB crystal structure 1khy (NTD) and 1qvr (for NBD1, MD, and NBD2). The domains were then rigid-body fit into the volume envelope generated from SAX/WAXS data of the Hsp104 hexamer in the presence of ATP. Top and side views are shown. The individual domains are color-coded: NTD (orange), NBD1 (light blue), MD (purple), and NBD2 (dark blue).

Movie S1. Hsp104 volume envelope reconstructions in the ATPγS, ADP-AlF$_x$, and ADP states. Related to Figure 4 and 5. Movie shows conformational changes of the Hsp104 hexamer and central channel from the ATPγS, ADP-AlFx, to ADP bound states.

Movie S2. Hsp104$^{\Delta N}$ volume envelope reconstructions in the ATPγS, ADP-AlF$_x$, and ADP states. Related to Figure 4 and 5. Movie shows conformational changes of the Hsp104$^{\Delta N}$ hexamer and central channel from the ATPγS, ADP-AlFx, to ADP bound states.

Table S1. Sweeny et al.

Substrate	**Hsp104 + ATPγS**	**$Hsp104^{\Delta N}$ + ATPγS**
Ure2 prions	65±6nM	55±8nM
Sup35 prions	51±4nM	45±11nM
NM4 prions	59±9nM	66±9nM
α-syn^{WT} amyloid	47±6nM	49±7nM
Q62 amyloid	56±8nM	63±7nM
Urea-denatured luciferase aggregates	49±3nM	55±6nM
FITC-casein (soluble)	55±7nM	194±60nM

Table S1. Apparent dissociation constants of Hsp104 and Hsp104$^{\Delta N}$ binding to various amyloid, disordered aggregate, and soluble substrates. Related to Figure 2. The apparent K_d of Hsp104 or Hsp104$^{\Delta N}$ binding the indicated amyloid, disordered aggregate, or soluble substrates in the presence of ATPγS. Values represent means±SD (n=3).

Hsp104 WT

			Guinier				GNOM					Porod		MM by Qr		GASBOR		Situs Dimensions		Channel				
	Location	Conc.	qmin	qRg range	Rg	I(O)	Angle range	Dmax	Rg	I(0)	Total Est.	Volume	P	Exp MM	Theor MM	No. Included	NSD	Damaver	Damfilt	Volume	Avg Diam	Max avg slice diam	Min avg slice diam	Slices
WT AMP-PNP	NSLS	2.5 mg/mL	0.01100	0.748-1.50	68.0 +- 0.0811	522.49 +- 0.644	0.0092-0.8290	255	69.2	526	0.774	1727702	3.9	645000	612000	10	2.588 +- 0.495	252x224x188.090	154x126x89.095					
	NSLS	5.0 mg/mL	0.01098	0.755-1.51	68.7 +- 0.0547	1011.5 +- 0.811	0.0073-0.8300	230	68.6	1010	0.671	1706347	3.9	650000	612000	9	2.373 +- 0.549	234x234x156.270	143x169x91.924	1.71E+05	29	56	0	90
	NSLS	2.9 mg/mL	0.01201	0.817-1.50	68.1 +- 0.0980	570.01 +- 0.835	0.0120-0.7950	235	68.2	567	0.652	1700962	3.9	624000	612000	9	2.366 +- 0.341	228x240x127.280	156x180x84.853					
WT ATPγS	NSLS	2.5 mg/mL	0.01101	0.754-1.51	68.5 +- 0.0739	530.51 +- 0.592	0.0097-0.7290	235	69.2	530	0.603	1711825	3.9	609000	612000	10	2.053 +- 0.266	221x234x156.271	130x143x91.924					
	NSLS	5.0 mg/mL	0.01100	0.756-1.51	68.7 +- 0.0518	1085.4 +- 0.824	0.0103-0.7290	235	69	1080	0.606	1708074	3.9	620000	612000	9	2.096 +- 0.169	237.5x225x150.261	150x137.5x88.388					
	SSRL	2.9 mg/mL	0.01497	1.04-1.53	69.4 +- 0.264	18.144 +- 0.0786	0.0140-0.4435	235	70.2	18	0.675	1660568	3.8		612000	9	2.267 +- 0.394	238x224x158.391	140x154x89.095					
	SSRL	5.9 mg/mL	0.01506	1.04-1.53	69.5 +- 0.209	35.650 +- 0.124	0.0140-0.4435	235	69.4	35	0.667	1647299	3.8		612000	9	2.173 +- 0.551	246.5x232x133.289	145x159.5x92.277					
	NSLS	1.5 mg/mL	0.01300	0.893-1.51	68.7 +- 0.108	318.88 +- 0.521	0.0110-0.7950	225	69	317	0.661	1654519	3.9	617000	612000	9	1.912 +- 0.292	216x228x144.25	156x156x84.853					
	NSLS	2.9 mg/mL	0.01300	0.909-1.54	69.9 +- 0.0832	616.75 +- 0.800	0.0110-0.7950	240	71.5	620	0.623	1692549	3.9	630000	612000	9	1.641 +- 0.114	228x228x135.765	168x156x93.338	1.05E+05	27.9	46.8	18	80
WT ATP	NSLS	2.5 mg/mL	0.01000	0.677-1.49	67.7 +- 0.0701	450.12 +- 0.458	0.0103-0.8290	220	67.1	445	0.684	1654371	3.9	631000	612000	10	2.034 +- 0.189	216x228x135.764	132x144x93.338					
	NSLS	5.0 mg/mL	0.01100	0.749-1.50	68.1 +- 0.0507	936.03 +- 0.685	0.0078-0.8100	230	68.2	935	0.599	1674270	3.9	640000	612000	9	2.013 +- 0.512	225x237.5x150.260	187.5x187.5x88.388	1.82E+05	38.2	50	28.4	95
	SSRL	2.9 mg/mL	0.01499	1.01-1.55	67.1 +- 0.241	17.190 +- 0.0683	0.0140-0.3171	230	67.1	17.1	0.657	1684247	3.9		612000	9	1.801 +- 0.203	237.5x237.5x141.422	187.5x175x97.227					
	SSRL	5.9 mg/mL	0.01493	1.01-1.56	67.5 +- 0.185	32.498 +- 0.100	0.0140-0.4435	230	67.1	32	0.662	1679654	3.9		612000	9	2.829 +- 0.653	234x221x165.463	143x143x101.117					
	NSLS	1.5 mg/mL	0.01000	0.670-1.54	67.0 +- 0.0871	242.38 +- 0.331									612000									
	NSLS	2.9 mg/mL	0.01099	0.736-1.54	66.9 +- 0.0862	444.53 +- 0.592	0.0110-0.7900	230	67.2	443	0.55	1654772	3.8	603000	612000	10	1.706 +- 0.080	216x228x135.764	156x168x93.338					
WT ADP-AlFx	SSRL	2.9 mg/mL	0.01498	0.981-1.51	65.4 +- 0.234	17.404 +- 0.0672	0.0140-0.4435	220	65	17.2	0.713	1642119	3.9		612000	9	2.412 +- 0.634	225x212.5x159.099	175x150x97.227					
	SSRL	5.9 mg/mL	0.01500	0.990-1.52	66.1 +- 0.188	33.300 +- 0.100	0.0140-0.4435	220	65.1	32.7	0.67	1641887	3.9		612000	9	2.343 +- 0.286	225x225x141.421	150x175x79.550					
	NSLS	1.5 mg/mL	0.02108	1.39-1.73	66.3 +- 0.228	306.67 +- 1.77	0.0210-0.7950	225	66.5	305	0.646	1593390	3.9		612000	9	1.806 +- 0.288	228x216x135.764	180x156x84.853					
	NSLS	2.9 mg/mL	0.02096	1.39-1.72	66.2 +- 0.145	586.1 +- 2.15	0.0210-0.7950	210	64.2	560	0.696	1625506	3.9		612000	10	2.108 +- 0.220	216x216x144.250	168x156x84.853					
	NSLS	5.0 mg/mL	0.01300	0.850-1.50	65.4 +- 0.298	1964.9 +- 9.52	0.0130-0.8000	220	63.9	1920	0.713	1580239	3.8	564000	612000	8	1.904 +- 0.132	216x228x135.764	180x180x93.338	6.51E+05	26.4	32.2	24.8	80
WT ADP	NSLS	2.5 mg/mL	0.01000	0.663-1.49	66.3 +- 0.0374	1365.4 +- 0.709	0.0078-0.8050	240	67	1370	0.636	1595855	3.8	617000	612000	9	2.004 +- 0.286	250x225x141.421	175x150x88.389	8.50E+04	27.1	40.3	14.5	75
	NSLS	5.0 mg/mL	0.01051	0.704-1.47	67.0 +- 0.0384	2807.5 +- 1.40	0.0078-0.7300	245	67.9	2820	0.601	1596676	3.9	622000	612000	9	2.034 +- 0.247	234x247x137.885	143x156x82.731					
	SSRL	2.9 mg/mL	0.01499	0.985-1.52	65.7 +- 0.225	16.606 +- 0.0616	0.0140-0.4435	210	64.8	16.3	0.723	1644595	3.9		612000	9	1.847 +- 0.193	207x218.5x138.24	172.5x195.5x105.712					
	SSRL	5.9 mg/mL	0.01499	0.994-1.53	66.3 +- 0.182	33.548 +- 0.100	0.0140-0.4435	215	64.6	32.6	0.731	1629344	3.8		612000	10	2.807 +- 0.487	216x216x200.465	135x148.5x95.460					
	NSLS	1.5 mg/ml	0.01201	0.799-1.53	66.6 +- 0.0935	287.34 +- 0.410	0.0120-0.7950	225	66.1	284	0.649	1610198	3.9	596000	612000	10	2.034 +- 0.245	216x228x144.250	168x168x84.852					
WT no nucleotide	NSLS	2.5 mg/mL	0.00750	0.538-1.51	71.7 +- 0.106	490.30 +- 0.773	0.0090-0.2240	245	71.6	487	0.646	1977362	3.8		612000	10	2.359 +- 0.158	243x243x152.736	148.5x148.5x85.914					
	NSLS	5.0 mg/mL	0.00899	0.616-1.49	72.5 +- 0.0647	971.03 +- 0.856	0.0090-0.1590	260	73.6	975	0.635	1979811	3.9		612000	9	2.663 +- 0.613	256.5x256.5x133.644	148.5x.148.5x95.460					
	SSRL	2.9 mg/mL	0.01497	1.09-1.53	72.8 +- 0.340	18.995 +- 0.105	0.0140-0.4435	255	73.3	18.9	0.746	2064711	3.9		612000	9	2.692 +- 0.958	256.5x256.5x152.736	162x175.5x85.914					
	SSRL	5.9 mg/mL	0.01501	1.11-1.56	74.2 +- 0.334	38.935 +- 0.214	0.0140-0.4384	255	74.7	38.7	0.764	2066202	3.9		612000	9	2.525 +- 0.676	243x256.5x143.190	175.5x229.5x105.006					
	NSLS	1.5 mg/mL	0.01400	0.990-1.49	70.7 +- 0.177	344.72 +- 0.945	0.0110-0.7950	225	70	341	0.701	2069872	3.8	668000	612000	9	2.530 +- 0.527	234x234x156.27	156x195x101.116	1.86E+05	26.5	56.5	16.5	100
	NSLS	2.9 mg/mL	0.01397	1.01-1.52	72.3 +- 0.116	688.30 +- 1.25	0.0110-0.7950	225	71.3	678	0.7	1969839	3.9		612000	9	2.714 +- 0.420	234x234x156.271	143x143x91.924					

Hsp104 dN

			Guinier				GNOM					Porod		MM by Qr		GASBOR		Situs Dimensions		Channel				
ΔN AMP-PNP	Location	Conc.	qmin	qRg range	Rg	I(O)	Angle range	Dmax	Rg	I(0)	Total Est.	Volume	P	Exp MM	Theor MM	No. Included	NSD	Damaver	Damfilt	Volume	Avg Diam	Max avg slice diam	Min avg slice diam	Slices
	NSLS	5.0 mg/mL	0.01150	0.768-1.50	66.8 +- 0.0553	869.53 +- 0.732	0.0118-0.7490	235	67.2	864	0.654	1521470	3.9	563000	506000	10	1.717 +- 0.069	228x240x118.794	144x156x67.882	7.80E+04	31.9	46.4	26.7	60
	NSLS	1.5 mg/mL	0.01000	0.651-1.50	65.1 +- 0.0976	254.35 +- 0.394	0.0100-0.7950	235	65.8	255	0.568	1441966	3.9	530000	506000	10	2.182 +- 0.167	237.5x237.5x123.743	175x187.5x70.711					
	NSLS	2.0 mg/mL	0.00801	0.523-1.50	65.3 +- 0.0822	339.88 +- 0.435	0.0080-0.7950	235	66.5	342	0.571	1455462	3.9	537000	506000	9	2.066 +- 0.182	240x240x118.794	204x204x67.883					
ΔN ATPγS	NSLS	2.5 mg/mL	0.01099	0.723-1.48	65.7 +- 0.0747	434.39 +- 0.492	0.0113-0.7890	235	67.1	434	0.61	1351120	3.9	523000	506000	9	1.661 +- 0.182	230x230x113.844	184x195.5x73.186					
	NSLS	5.0 mg/mL	0.01100	0.733-1.50	66.6 +- 0.0610	933.47 +- 0.851	0.0113-0.7860	235	68	933	0.606	1441596	3.9	538000	506000	9	1.726 +- 0.235	241.5x230x113.844	172.5x149.5x73.186					
	SSRL	2.3 mg/mL	0.01398	0.996-1.50	71.2 +- 0.290	16.918 +- 0.780	0.0140-0.2414	220	69.6	8.25	0.681	1543621	3.9		506000									
	SSRL	4.6 mg/mL	0.01399	0.970-1.53	69.4 +- 0.336	8.3718 +- 0.470	0.0150-0.2515	220	69.6	16.1	0.628	1571916	3.9		506000									
	NSLS	1.5 mg/mL	0.01200	0.787-1.51	65.6 +- 0.0864	298.48 +- 0.392	0.0120-0.7950	220	66	295	0.589	1335332	3.9	515000	506000	9	1.338 +- 0.072	198x209x116.672	154x154x77.782	5.70E+04	21.6	24.7	15.7	80
	NSLS	2.0 mg/mL	0.01200	0.790-1.52	65.9 +- 0.0904	404.09 +- 0.565	0.0120-0.7950	220	66.4	400	0.616	1328161	3.9	520000	506000	9	1.458 +- 0.227	209x209x108.894	143x154x77.782					
ΔN ATP	NSLS	2.5 mg/mL	0.00650	0.712-1.49	64.8 +- 0.0769	379.69 +- 0.454	0.0068-0.7900	240	67.2	387	0.504	1353560	3.9	512000	506000	9	1.899 +- 0.116	230x241.5x105.713	195.5x195.5x73.185					
	NSLS	5.0 mg/mL	0.01100	0.717-1.50	65.2 +- 0.0491	862.45 +- 0.638	0.0113-0.7900	235	65.9	859	0.571	1436818	3.9	519000	506000	9	1.757 +- 0.176	230x207x113.844	184x149.5x65.054	1.25E+05	33.75	60.9	24.2	70
	SSRL	2.3 mg/mL	0.01499	0.957-1.54	63.8 +- 0.276	7.0681 +- 0.033	0.0140-0.2919	225	64.6	7.08	0.779	1382322	3.9		506000	9	1.645 +- 0.135	230x230x121.976	195.5x172.5x81.317					
	SSRL	4.6 mg/mL	0.01499	0.972-1.50	64.8 +- 0.238	13.913 +- 0.534	0.0140-0.2919	225	65.1	13.8	0.674	1364062	3.9		506000	10	1.419 +- 0.036	230x218.5x105.712	207x207x73.186					
	NSLS	1.5 mg/mL	0.01000	0.629-1.51	62.9 +- 0.0795	220.52 +- 0.277	0.0110-0.7950	230	63.4	221	0.488	1348699	3.9	478000	506000									
	NSLS	2.0 mg/mL	0.01000	0.629-1.51	62.9 +- 0.0792	220.94 +- 0.276	0.0110-0.7950	240	63.8	222	0.481	1349023	3.9	468000	506000									
ΔN ADP-AlFx	SSRL	2.3 mg/mL	0.01399	0.852-1.53	60.9 +- 0.249	6.9066 +- 0.0289	0.0140-0.2666	205	60.9	6.9	0.689	1237425	3.8		506000	9	1.466 +- 0.245	210x199.5x96.52	189x168x81.671					
	SSRL	4.6 mg/mL	0.01397	0.869-1.50	62.2 +- 0.194	13.553 +- 0.0428	0.0140-0.4435	215	62.7	13.6	0.683	1325795	3.9		506000	9	1.462 +- 0.074	220x209x108.894	209x187x70.004					
	NSLS	1.5 mg/mL	0.01899	1.20-1.52	63.2 +- 0.271	251.55 +- 1.41	0.0190-0.7950	220	62.2	246	0.664	1416628	3.9	527000	506000	10	1.538 +- 0.074	209x209x116.673	154x154x62.225					
	NSLS	2.0 mg/mL	0.01897	1.21-1.53	63.8 +- 0.228	337.34 +- 1.60	0.0190-0.7950	220	63.7	334	0.685	1408572	3.9	544000	506000	9	1.421 +- 0.056	209x209x108.895	165x165x70.003					
	NSLS	5.0 mg/mL	0.01400	0.889-1.52	63.5 +- 0.298	1556.8 +- 7.92	0.01400-0.800	220	62.5	1530	0.84	1309244	3.9	488000	506000	9	1.832 +- 0.259	220x220x108.895	176x176x70.004	1.51E+05	30.4	53.1	23.4	65
ΔN ADP	NSLS	2.0 mg/mL	0.00749	0.465-1.52	62.0 +- 0.0933	228.15 +- 0.370	0.0078-0.7850	233	63.5	229	0.624	1226602	3.8	476000	506000	9	1.688 +- 0.216	209x220x108.894	165x176x70.004					
	NSLS	4.0 mg/mL	0.01100	0.695-1.49	63.2 +- 0.0665	498.94 +- 0.537	0.0113-0.7860	225	63.8	496	0.605	1257546	3.9	490000	506000	9	1.523 +- 0.076	231x209x108.895	187x176x70.003	9.30E+04	26.4	49.5	14.7	70
	SSRL	2.3 mg/mL	0.01499	0.921-1.54	61.4 +- 0.241	6.7263 +- 0.0282	0.0140-0.2414	220	62.6	6.77	0.66	1239575	3.9		506000									
	SSRL	4.6 mg/mL	0.01500	0.941-1.51	62.7 +- 0.209	13.284 +- 0.0456	0.0140-0.3374	230	63.9	13.4	0.789	1261388	3.9		506000									
	NSLS	1.5 mg/mL	0.01501	0.960-1.54	64.0 +- 0.121	245.70 +- 0.525	0.0150-0.7950	230	64.4	244	0.611	1364382	3.9	512000	506000									
	NSLS	2.0 mg/mL	0.01500	0.963-1.54	64.2 +- 0.102	320.01 +- 0.575	0.0150-0.7950	225	64.5	318	0.614	1356323	3.9	513000	506000									
ΔN no nucleotide	NSLS	2.5 mg/mL	0.00800	0.584-1.50	72.9 +- 0.154	395.38 +- 0.881	0.0083-0.7890	245	72.7	388	0.671	1847354	3.9	497000	506000	9	1.675 +- 0.093	230x230x113.844	161x172.5x65.054	1.28E+05	47	52.3	41.7	60
	NSLS	5.0 mg/mL	0.01151	0.917-1.52	79.7 +- 0.117	956.06 +- 1.56	0.0118-0.7890	240	75.5	882	0.631	2180685	3.9	567000	506000									
	SSRL	2.3 mg/mL	0.01497	1.10-1.54	73.2 +- 0.469	8.5800 +- 0.0659	0.0140-0.2919	235	72.2	8.36	0.807	1903839	3.8		506000									
	SSRL	4.6 mg/mL	0.01497	1.16-1.55	77.5 +- 0.490	17.835 +- 0.0141	0.0140-0.4435	235	74.4	16.7	0.727	1944172	3.9		506000									
	NSLS	1.5 mg/mL	0.01399	1.00-1.50	71.5 +- 0.153	328.19 +- 0.792	0.0140-0.7950	230	70.6	321	0.688	1933427	3.9	529000	506000									
	NSLS	2.0 mg/mL	0.01299	0.938-1.52	72.2 +- 0.123	435.05 +- 0.815	0.0130-0.7950	240	71.8	429	0.682	2251878	3.9	536000	506000									

Samples shaded in blue are the ones used in the final reconstructions

Table S2. Parameters derived from SAXS/WAXS of WT Hsp104 and Hsp104. Related to Figure 4 and 5. R_g values from the Guinier region of the scattering curves were determined using the program PRIMUS (Konarev et al., 2003). Distance distribution functions P(r) were calculated by the program GNOM using an indirect Fourier transform (Svergun 1992). The maximum dimension of the particle (Dmax) was determined by examining the quality of fit to the experimental data for a Dmax range of 180 to 280 Å varied in 5Å increments. Values for R_g were computed from the second moment of the P(r). The Porod volume and p value were calculated by the java-based program ScÅtter (www.bioisis.net/tutorial/9). The mass of the particle was calculated from Qr as described (Rambo and Tainer, 2013). GASBOR (Svergun et al. 2001) was run on the raw scattering data and DAMAVER (Volkov and Svergun, 2003) used to avergae the envelopes and calculate normalized spatial discrepancy (NSD). Damaver and damfilt pdb files were converted using the program pdb2vol from the SITUS suite of programs (Wriggers et al., 2011). Channel dimensions of the reconstructed volumes were determined using MATLAB. See also Extended Experimental Procedures.

Nucleotide	WT R_g	WT D_{max}	ΔN R_g	ΔN D_{max}
AMP-PNP	68.7 ± 0.3	240 ± 8	66.5 ± 0.4	235 ± 0
ATPγS	69.7 ± 0.4	234 ± 2	67.8 ± 0.6	225 ± 3
ATP	67.3 ± 0.2	228 ± 2	65.7 ± 0.6	231 ± 4
ADP-AlF_x	64.9 ± 0.5	219 ± 2	62.2 ± 0.4	213 ± 3
ADP	66.1 ± 0.6	227 ± 7	63.8 ± 0.3	227 ± 2
No Nucleotide	72.4 ± 0.7	244 ± 6	72.9 ± 0.7	238 ± 2

Table S3. Average R_g and D_{max} values from GNOM analysis of SAXS data. Related to Figure 4 and 5. Distance distribution functions, P(r), were calculated by the program GNOM using an indirect Fourier transform (Svergun, 1992). The maximum dimension of the particle (D_{max}) was determined by examining the quality of fit to the experimental data for a D_{max} range of 180 to 280Å, varied in 5Å increments. Values for R_g were computed from the second moment of the P(r). Values reported are averaged from scattering data collected at various concentrations and beamlines (See Extended Experimental Procedures for beamline details). Full details of each sample are given in Table S2.

Extended Experimental Procedures

Proteins

Hsp104 variants were generated by Quikchange Site-Directed Mutagenesis (Agilent). Hsp104, Hsp104^{DPL} (Y257A:Y662A), Hsp104$^{\Delta N}$ (Hsp104 lacking amino acids 1-156), Hsp104$^{\Delta NDPL}$ (Δ1-156:Y257A:Y662A), and HAP were purified as described (DeSantis et al., 2014; Sweeny et al., 2011). Sup35, Ure2, Q62, α-syn, ClpP, GroEL$_{TRAP}$, Sse1, Ssa1, and Sis1 were purified as described (DeSantis et al., 2012; Doyle et al., 2007; Jackrel et al., 2014; Shorter and Lindquist, 2006). NM, NM-GFP, and single cysteine NM variants were purified as described (Krishnan and Lindquist, 2005). Single cysteine NM mutants were labeled with either pyrene maleimide (N-(1-pyrene)maleimide; Life Technologies), acrylodan (6-acryloyl-2-dimethylaminonaphthalene; Life Technologies), BPMTS (benzophenone-4-carboxamidocysteine methanethiosulfonate; Toronto Research Chemicals Inc.), or crosslinked with BMB (1,4-bis-maleimidobutane; Thermo Scientific Pierce) under denaturing conditions as described (Krishnan and Lindquist, 2005). Hsc70, Hsp72, and Hdj2 were from Enzo Life Sciences. Firefly luciferase and FITC-casein were from Sigma. Creatine kinase was from Roche. Purity of all proteins was determined by SDS-PAGE and Coomassie staining to be > 95%. Unless otherwise stated Hsp104 concentrations refer to the hexamer.

Size-exclusion chromatography coupled to multi-angle light scattering (SEC MALS)

The absolute molecular weights of the apo hexamers of Hsp104 and Hsp104$^{\Delta N}$ (15μM monomer) were determined using multi-angle light scattering coupled with refractive interferometric detection (Wyatt Technology Corporation) and a TSK4000 size-exclusion column. The column was equilibrated with 20mM TrisHCl pH 7.4, 140mM KCl and 10mM $MgCl_2$ at room temperature and elution of Hsp104 was monitored by both absorbance at 280nm and refractive index.

ATPase and GTPase activity

Hsp104 variants (0.25μM monomer) were incubated for 5min or 10min at 25°C with ATP (1mM) in luciferase refolding buffer (LRB: 25mM HEPES-KOH pH 7.4, 150mM KAOc, 10mM MgAOc, 10mM DTT). ATPase activity was assessed using a malachite green phosphate detection kit (Innova). Sup35 GTPase activity was measured as described (Krzewska et al., 2007).

Luciferase reactivation in vitro

Luciferase aggregation and reactivation were performed as described (DeSantis et al., 2012; Glover and Lindquist, 1998). Briefly, firefly luciferase (50μM) was incubated in LRB with 8M urea at 30°C for 30min to form aggregates. After a rapid 100-fold dilution in LRB, the aggregates were flash frozen and stored at -80°C until use. Reactivation assays were performed with Hsp104 (1μM), Hsp70 (Hsc70 or Hsp72 at 1μM), Hsp40 (Hdj2, 1μM), 5.1mM ATP, and an ATP regeneration system (1mM creatine phosphate, 0.25μM creatine kinase) for 90min at 25°C. Alternatively, Hsp70, Hsp40 and 5.1 mM ATP were replaced with 5.1mM nucleotide of different ratios of ATP:ATPγS. Luciferase activity was assessed using a luciferase assay system from Promega. Luminescence was measured on a Tecan Infinite M1000 or Safire^2 plate reader.

Luciferase reactivation in vivo

Luciferase reactivation in vivo was performed as described (DeSantis et al., 2014). Briefly, W303 Δ*hsp104* (*MATa, can1-100, his3-11,15, leu2-3,112, trp1-1, ura3-1, ade2-1, hsp104:kanMX4*) yeast cells harboring pGPD-LuxAB (encoding a temperature-sensitive luciferase fusion protein) and empty centromeric pHSE vector, pHSE-Hsp104, or pHSE-Hsp104$^{\Delta N}$ were grown to mid-log phase in SD-his-ura liquid. Matched cultures were preincubated at 37°C for 30min and then incubated at 44°C for 50min. Cycloheximide (10μg/ml) was then added and cultures were incubated for a further 10min at 44°C. Cells were then shifted to 30°C and luciferase activity was measured at 0, 90, and 120min. Luciferase activity was expressed as the percentage of the Hsp104 condition after 120min

Thermotolerance

Yeast thermotolerance assays were performed as described (DeSantis et al., 2014). Briefly, W303aΔ*hsp104* (*MATa, can1-100, his3-11,15, leu2-3,112, trp1-1, ura3-1, ade2-1, hsp104:kanMX4*) yeast were transformed with a centromeric pHSE plasmid encoding

Hsp104, Hsp104$^{\Delta N}$, or the empty vector control. The strains were grown in SD-ura media to an A_{600} of 0.5, and incubated at 37°C for 30min to induce Hsp104 expression. Cells were then heat shocked for 0-20min at 50°C, immediately transferred to ice for 2min, and then plated on SD-ura plates, and after a 2-day incubation at 30°C colonies were counted using an acolyte automated colony counter (Synbiosis). Immunoblotting was used to confirm expression levels of Hsp104.

Amyloid and prion disaggregation

Sup35, NM-GFP, and Ure2 prions were assembled in assembly buffer (AB: 40mM HEPES-KOH pH 7.4, 150mM KCl, 20mM $MgCl_2$ and 1mM DTT) plus 10% (v/v) glycerol as described (Shorter and Lindquist, 2006). For Sup35, GTP (1mM) was included to stabilize the C-terminal GTP binding domain. Q62 fibrils and α-syn fibrils were assembled in AB as described (DeSantis et al., 2012). Preformed Sup35 or Ure2 prions, or Q62 or α-syn amyloid (1μM monomer) were treated with Hsp104 (0.03μM, 1μM, or 10μM) or Hsp104$^{\Delta N}$ (1μM or 10μM) plus Ssa1 (1μM), Sse1 (1μM), Sis1 (1μM), ATP (5mM), and ATP regeneration system (1mM creatine phosphate, 0.25μM creatine kinase) for 6h at 25°C. For experiments with NM-GFP prions, NM-GFP prions (2.5μM) were treated with Hsp104 (1μM) plus GroEL$_{TRAP}$ (1.5μM), Ssa1 (1μM), Sse1 (1μM), and Sis1 (1μM) for 0-60min at 25°C. At the indicated times, GFP fluorescence was measured (excitation: 395nm; emission: 510nm). Fibril integrity was determined by the fluorescence of the amyloid-diagnostic dye Thioflavin-T (ThT) (excitation: 450 nm; emission: 482 nm) as described (Krishnan and Lindquist, 2005). Alternatively, fibril integrity was determined by sedimentation analysis: reactions were centrifuged at 100,000g for 10min at 25°C. The amount of soluble protein (Sup35, Ure2, Q62, or α-syn) in the supernatant fraction was then determined via immunoblot. For electron microscopy (EM), disassembly reactions were spotted onto 300-mesh-formvar carbon-coated EM grids. The samples were allowed to adhere to the grid for 2min before being negatively stained with 2% uranyl acetate for 2min and rinsed with milli-Q distilled water. Micrographs were captured using a transmission electron microscope (JEOL 1010, Jeol USA).

Hsp104 and Hsp104$^{\Delta N}$ substrate binding

The apparent K_d of Hsp104 or Hsp104$^{\Delta N}$ binding the indicated amyloid, disordered aggregate, or soluble substrate in the presence of ATPγS (1mM) was determined as described (DeSantis et al., 2012; Jackrel et al., 2014).

Sup35 prionogenesis

For spontaneous, unseeded prionogenesis, Sup35 (2.5μM) was incubated in AB plus 10% glycerol and 1mM GTP for 0-8h at 25°C with rotation (80rpm on a mini-rotator, Glas-Col) in the absence or presence of Hsp104 (0.03μM or 1μM) or Hsp104$^{\Delta N}$ (0.03μM, 1μM, or 5μM) plus ATP (5mM) and ATP regeneration system (1mM creatine phosphate, 0.25μM creatine kinase). Prionogenesis was assessed by ThT fluorescence as above. The oligomer-specific A11 antibody was used to detect prionogenic Sup35 oligomers via ELISA as described (Kayed et al., 2003). Seeded assembly was unagitated and performed for the indicated time at 25°C. The amount of seed was 2% (wt/wt). In some seeded reactions, ATP (5mM) was replaced with AMP-PNP (5mM). In some reactions, Sup35 prions (2.5μM), or NM prions (2.5μM monomer) stapled by a BMB crosslink in the Head (N21C) or Tail (G96C) region were treated with His_6-Hsp104 (0.03μM or 1μM) or His_6-Hsp104$^{\Delta N}$ (0.03μM, 1μM, or 5μM) plus Ssa1 (1μM), Sse1 (1μM), Sis1 (1μM), ATP (5mM), and ATP regeneration system (1mM creatine phosphate, 0.25μM creatine kinase) for 1h at 25°C. Reactions were then depleted of His_6-Hsp104 as described (Shorter and Lindquist, 2004) and used to seed (2% wt/wt) fresh, undisturbed Sup35 (2.5μM) prionogenesis.

Sup35 prion transformation

Yeast cells from a W303-derived strain (*MATα leu2-3, -112 his3-11 trp1-1 ura3-1 ade1-14 can1-100* [*rnq*$^-$] [*psi*$^-$] [*ure-o*]) that contained an ADE1 nonsense mutation suppressible by [*PSI*$^+$] were transformed with the indicated Sup35 conformers and a URA3 plasmid. The proportion of Ura^+ transformants that acquired [*PSI*$^+$] was determined as described (Krishnan and Lindquist, 2005).

Site-resolved pyrene and acrylodan fluorescence

Single cysteine NM variants (5μM) bearing pyrene or acrylodan labels at the indicated position were assembled into prions in AB at 4°C or 25°C with agitation at 1,400rpm (Eppendorf thermomixer). Pyrene and acrylodan fluorescence were monitored as described (Krishnan and Lindquist, 2005; Roberts et al., 2009).

Site-resolved BPMTS crosslinking

Single cysteine NM variants (10μM) bearing benzophenone-4-carboxamidocysteine methanethiosulphonate (BPMTS) at the indicated position were assembled into prions in AB without DTT at 4°C with agitation at 1,400rpm (Eppendorf thermomixer) in the dark. Prionogenesis was confirmed by ThT fluorescence and ability to infect [*psi*$^-$] yeast cells. BPMTS-labeled NM4 prions (2.5μM) were then incubated with Hsp104 or Hsp104$^{\Delta N}$ (5μM) plus ATPγS (5mM) or ADP (5mM) for 10min at 4°C. Crosslinking was then elicited by UV irradiation at 365nm for 20min. Omission of UV irradiation at this step served as the no crosslinking control. NM4 prions were then separated from soluble Hsp104 or Hsp104$^{\Delta N}$ by centrifugation (100,000g, 10min, 4°C), followed by washes with AB (without DTT) plus ADP (5mM) and AB (without DTT) plus 1M KCl to remove any uncrosslinked Hsp104. Samples were then processed for reducing SDS-PAGE (which cleaves the crosslink) and quantitative immunoblot to detect Hsp104 using an anti-Hsp104 polyclonal antibody (ADI-SPA-1040, Enzo Life Sciences). The Hsp104 binding site on NM4 prions defined by our studies is in accord with those suggested by peptide array studies (Helsen and Glover, 2012).

FITC-casein degradation assay

FITC-casein degradation assays were performed as described (Jackrel et al., 2014; Tessarz et al., 2008). Briefly, FITC-casein (100nM-60μM) was incubated with HAP variants (1μM), ClpP (21μM monomer), 5.1mM ATP and an ATP regenerating system in LRB for 60min at 25°C. Degradation of FITC-casein was monitored by measuring fluorescence of free FITC (excitation: 490nm; emission: 520 nm) using a Tecan Infinite M1000 or Safire^2 plate reader. Degradation rates were plotted against FITC-casein concentration to determine K_m and V_{max}.

$RepA_{1\text{-}70}$-GFP unfolding assay

$RepA_{1\text{-}70}$-GFP unfolding assays were performed as described (Doyle et al., 2007; Jackrel et al., 2014). Briefly, $RepA_{1\text{-}70}$-GFP (0.7μM) was treated with Hsp104 or $Hsp104^{\Delta N}$ (1μM) plus either 2.5mM ATP and 2.5mM ATPγS (1:1) or 3.33mM ATP and 1.67mM ATPγS (2:1), $GroEL_{TRAP}$ (1.5μM), 0.02mg/ml BSA, and 0.005% (v/v) Triton-X100 and an ATP regenerating system (1mM creatine phosphate, 0.25μM creatine kinase) in LRB. The decrease in fluorescence (excitation: 395 nm; emission: 510 nm) over a period of 60min was monitored using a Tecan Infinite M1000.

Small- and wide-angle x-ray scattering (SAXS/WAXS)

X-ray scattering data were collected at beamline 4-2 at the Stanford Synchrotron Radiation Laboratory (SSRL, Menlo Park, CA), and beamline X9 at the National Synchrotron Light Source (NSLS, Upton, NY) (details specific to each beamline are provided below). Data were collected at multiple concentrations between 1.5mg/ml and 6mg/ml. Samples were oscillated in quartz capillaries during data collection to minimize radiation damage. The two-dimensional scattering images were collected on CCD detectors, and circularly averaged using software developed at the individual beamlines to yield one-dimensional scattering profiles as a function of momentum transfer q (in $Å^{-1}$, where $q=4\pi\sin(\theta)/\lambda$, where 2π is the scattering angle and λ is the wavelength). The raw scattering data were scaled and buffer subtracted using the program PRIMUS (Konarev et al., 2003). Each individual scattering profile was visually inspected for radiation damage and aggregation prior to averaging, including Guinier and Kratky plot analysis. For data collected at NSLS, where both SAXS and WAXS data are collected on separate detectors simultaneously, averaged scattering profiles from the SAXS and WAXS detectors were scaled and merged in PRIMUS to yield a composite profile encompassing all of the recorded scattering angles. The parameters derived from classical Guinier analysis (Rice, 1956) (R_g, and I(0)) corresponded well with those derived from distance distribution functions. P(r) were calculated by the program GNOM (Svergun, 1992) using the indirect Fourier transform. The maximum dimension of the particle (D_{max}) was determined by examining the quality of fit to the experimental data for a D_{max} range of 180Å to 280Å, varied in 5Å increments. Fits were optimized by three criteria: (1) maximizing the Total

Estimate metric; (2) minimization of the discrepancy between calculated and experimental profiles; and (3) optimizing the visual properties of the shape distribution function. The Porod volume and Porod exponent values were calculated by the Java-based program ScÅtter (http://www.bioisis.net/tutorial/9). The mass of the particle was confirmed by Qr calculations, as previously described (Rambo and Tainer, 2013).

SAXS data were collected at beamline 4-2 at the Stanford Synchrotron Radiation Laboratory (SSRL, Menlo Park, CA) at room temperature with a sample to detector distance of 1600mm. Using software developed at the beamline, two-dimensional scattering profiles collected using a Rayonix MX225-HE detector were converted into one-dimensional intensity profiles. The x-ray wavelength was 1.2Å, providing an accessible q where $0.0140<q<0.4435Å^{-1}$. The protein samples and matching buffer solutions, 30μl for each measurement, were exposed for ten 10s exposures in a 1.2mm path capillary with thin mica windows sealed across the evacuated flight path with oscillation. Each exposure was checked for radiation damage by the automated software prior to averaging. After each measurement the capillary was washed thoroughly and purged with compressed nitrogen.

SAXS and WAXS data were collected simultaneously at beamline X9 at the National Synchrotron Light Source (NSLS, Upton, NY) at 10°C, or 25°C for the ADP-AlF_x state, by two overlapping detectors, a Mar 165 CCD SAXS detector 3.4m from the sample, and a custom built Photonic Science CCD WAXS detector. The two-dimensional images were converted into one-dimensional scattering profiles using software developed at the beamline. The x-ray wavelength was 0.855Å. Between the two detectors configurations, an accessible q of $0.0055<q<1.0Å^{-1}$ was achieved. Data to q_{max} of $0.795Å^{-1}$ was used for data analysis and reconstructions. The sample cell contained a glass capillary sealed across the evacuated chamber. The protein samples and matching buffer solutions were flowed through the capillary and oscillated during exposure to reduce radiation damage. For data collection 30μl of the protein sample or matching buffer solution was exposed for 180s, subdivided into three 60s exposures of 10μl. Our SAXS data will be deposited at BioIsis.net upon publication.

Shape reconstructions from SAXS/WAXS data

Shape reconstructions of the hexamer were generated using the program GASBOR (Svergun et al., 2001). Information required for GASBOR modeling is the x-ray scattering profile, the number of residues to be modeled (GASBOR assigns a dummy reside to represent each residue), and the D_{max}. Six-fold symmetry was imposed. Since each inverse scattering has no one unique solution, GASBOR calculations were performed ten times using all of the recorded scattering data to q_{max} of 0.7-0.8 $Å^{-1}$; GASBOR calculations using q_{max} truncated to 0.5$Å^{-1}$ or calculations with the program DAMMIN/F yielded similar results. Regions that are flexible are assigned different positions in individual simulations. The ten independent dummy residue reconstructions were aligned and scored based on the normalized spatial discrepancy (NSD) (Kozin and Svergun, 2001). The individual reconstructions were only included if their NSD < mean NSD + 2 * variation. The included reconstructions were averaged and filtered to yield a final most-probable model using the DAMAVER suite of programs (Svergun and Koch, 2003; Volkov and Svergun, 2003). The individual bead models were visualized in PyMOL (http://www.pymol.org). The filtered and unfiltered average models were converted to volume envelopes using SITUS (Wriggers et al., 1999) and visualized using Chimera (Pettersen et al., 2004).

Channel reconstructions from SAXS/WAXS data

The SITUS maps were converted to MRC-format maps using map2map, part of the SITUS suite of programs (Wriggers et al., 1999). The three-dimensional electron density file in the MRC format was imported into Matlab (Mathworks) using a custom script, which parses the file into a three-dimensional matrix of electron density. The read function also extracts the voxel dimensions to scale the measurement. The built in Matlab function "edge" was used to find the edges of two-dimensional slices of the electron density using the Sobel method. The Sobel method finds the edges by approximating the first derivative over the image; maxima of the first derivative are edges.

The density matrix was oriented such that the Z-axis moved through the central channel of the Hsp104 hexamer. Two-dimensional X-Y slices are torroidal slices of the density where the central cavity is the channel. A custom script was used to find edges for each two-dimensional slice of the density matrix. The X, Y and Z coordinates of each edge point were stored in an array and were scaled by the voxel dimensions. This array can be interpreted as a list of three-dimensional vectors that all point from one corner of the density matrix (0,0,0) to voxels, which lie upon the edge of the channel. The built in Matlab function "convhulln" was used to convert the vector array into a convex hull and measured the volume of the hull. The convex hull is the shell of the channel and the volume is the volume of the Hsp104 hexamer channel.

A distance was measured for each slice of the channel to determine its width. First, edges were found for each slice using the Matlab function "edge". Two mid-lines of the channel were extracted, one horizontal and one vertical, and the scaled distance from edge to edge was measured. The two-dimensional slice was then rotated over 45 degrees in 5 degree increments for a total of 18 channel width measurements of each two-dimensional slice. The average of the 18 channel width measurements is reported. The algorithm was then iterated over every Z-slice of the density to measure the channel widths through the channel. We have made the custom scripts generated for measuring channel width and volume from SAXS MRC files available at: http://www.mathworks.com/matlabcentral/fileexchange/47095-saxs-channel-width-and-volume-measurement

Mutant doping studies

Here, mutant Hsp104 subunits with specific defects (e.g. substrate translocation) are mixed with WT subunits to generate heterohexamer ensembles. Incorporation of mutant subunits into hexamers occurs according to a binomial distribution dictated by the WT:mutant ratio (Figure 6A) (DeSantis et al., 2012; Werbeck et al., 2008). Theoretical activities for each ratio of WT:mutant can be determined based on the fraction of each type of heterohexamer present and how many active subunits per hexamer are required for activity (Figure 6A, B) (DeSantis et al., 2012; Werbeck et al., 2008). If cooperativity is dispensable, then only one WT subunit per hexamer is required, and a linear decrease in activity is expected (Figure 6B, orange line) (DeSantis et al., 2012). If global cooperativity (i.e. one mutant subunit per hexamer eliminates activity) were required, a steep decline in activity is expected (Figure 6B, blue line), and if sub-global cooperativity (i.e. 2-5 mutant subunits per hexamer ablate activity) were required, an intermediate curve is anticipated (Figure 6B) (DeSantis et al., 2012). Luciferase reactivation was performed as above except prior to addition to the reaction Hsp104 was mixed with Hsp104^{DPL}, and, Hsp104$^{\Delta N}$ was mixed with Hsp104$^{\Delta NDPL}$ in the following ratios: 6:0, 5:1, 4:2, 3:3, 2:4, 1:5, 0:6 and incubated for 30min on ice. NM25 prion disaggregation was monitored as above except that prior to addition to the reaction Hsp104 was mixed with Hsp104$^{\Delta N}$ in the following ratios: 6:0, 5:1, 4:2, 3:3, 2:4, 1:5, 0:6 and incubated for 30min on ice.

Yeast proteinopathy models

W303aΔ*hsp104* (*MATa, can1-100, his3-11,15, leu2-3,112, trp1-1, ura3-1, ade2-1, hsp104:kanMX4*) yeast strains integrated with galactose-inducible TDP-43, FUS, or α-syn were transformed with the indicated galactose-inducible Hsp104 variant or vector control as described (Jackrel et al., 2014). For the spotting assays, yeast were grown to saturation overnight in raffinose supplemented dropout media at 30°C. Cultures were diluted and normalized to A_{600nm}, grown to an A_{600nm}=2.0, serially diluted, and spotted in duplicate onto synthetic dropout media containing glucose or galactose. Plates were analyzed after growth for 2-3 days at 30°C. Select strains were induced for 5h, lysed, and immunoblotted for Hsp104 to assess expression level as described (Jackrel et al., 2014). 3-Phosphoglycerate kinase (PGK) serves as a loading control. Fluorescence microscopy of yeast co-expressing α-syn-YFP or FUS-GFP and the indicated Hsp104 variant or vector was performed as described (Jackrel et al., 2014) except that images were captured using LAF software (Leica) with a charge-coupled device camera (ORCA AG; Hamamatsu Photonics) mounted on an inverted microscope (DMI6000B Leica) with a 100X objective. α-syn localization was quantified by counting the number of cells containing plasma membrane fluorescence or cytoplasmic aggregates. FUS localization was quantified by counting the number of cells containing foci or diffuse fluorescence.

Supplemental References

Doyle, S.M., Shorter, J., Zolkiewski, M., Hoskins, J.R., Lindquist, S., and Wickner, S. (2007). Asymmetric deceleration of ClpB or Hsp104 ATPase activity unleashes protein-remodeling activity. Nat. Struct. Mol. Biol *14*, 114-122.

Glover, J.R., and Lindquist, S. (1998). Hsp104, Hsp70, and Hsp40: a novel chaperone system that rescues previously aggregated proteins. Cell *94*, 73-82.

Helsen, C.W., and Glover, J.R. (2012). Insight into molecular basis of curing of [PSI+] prion by overexpression of 104-kDa heat shock protein (Hsp104). J Biol Chem *287*, 542-556.

Kayed, R., Head, E., Thompson, J.L., McIntire, T.M., Milton, S.C., Cotman, C.W., and Glabe, C.G. (2003). Common structure of soluble amyloid oligomers implies common mechanism of pathogenesis. Science *300*, 486-489.

Konarev, P.V., Volkov, V.V., Sokolova, A.V., Koch, M.H.J., and Svergun, D.I. (2003). PRIMUS: a Windows PC-based system for small-angle scattering data analysis. J. Appl. Cryst. *36*, 1277-1282.

Kozin, M.B., and Svergun, D. (2001). Automated matching of high- and low-resolution structural models. J. Appl. Cryst. *34*, 33-41.

Pettersen, E.F., Goddard, T.D., Huang, C.C., Couch, G.S., Greenblatt, D.M., Meng, E.C., and Ferrin, T.E. (2004). UCSF Chimera--a visualization system for exploratory research and analysis. J. Comput. Chem. *25*, 1605-1612.

Rambo, R.P., and Tainer, J.A. (2013). Accurate assessment of mass, models and resolution by small-angle scattering. Nature *496*, 477-481.

Rice, S.A. (1956). Small angle scattering of X-rays. A. Guinier and G. Fournet. Translated by C. B. Wilson and with a bibliographical appendix by K. L. Yudowitch. Wiley, New York, 1955. J. Polym. Sci. *19*, 594-594.

Roberts, B.E., Duennwald, M.L., Wang, H., Chung, C., Lopreiato, N.P., Sweeny, E.A., Knight, M.N., and Shorter, J. (2009). A synergistic small-molecule combination directly eradicates diverse prion strain structures. Nat. Chem. Biol. *5*, 936-946.

Shorter, J., and Lindquist, S. (2004). Hsp104 catalyzes formation and elimination of self-replicating Sup35 prion conformers. Science *304*, 1793-1797.

Svergun, D.I., Petoukhov, M.V., and Koch, M.H. (2001). Determination of domain structure of proteins from X-ray solution scattering. Biophys. J. *80*, 2946-2953.

Sweeny, E.A., DeSantis, M.E., and Shorter, J. (2011). Purification of Hsp104, a protein disaggregase. J. Vis. Exp. *55*, e3190.

Tessarz, P., Mogk, A., and Bukau, B. (2008). Substrate threading through the central pore of the Hsp104 chaperone as a common mechanism for protein disaggregation and prion propagation. Mol. Microbiol. *68*, 87-97.

Werbeck, N.D., Schlee, S., and Reinstein, J. (2008). Coupling and dynamics of subunits in the hexameric AAA+ chaperone ClpB. J Mol Biol *378*, 178-190.